Identification of *STMN1* as a lactylation-related driver of lung cancer progression using Mendelian randomization

YIFAN CAI[1-3*], YUCHENG ZHONG[4*], HONGLIN WANG[5*], SHUANG ZHU[1-3], FANG HUANG[1-3], QIUYUE ZHANG[1-3] and SHAOBO HU[6]

[1]Cancer Center, Union Hospital, Tongji Medical College, Huazhong University of Science and Technology, Wuhan, Hubei 430022, P.R. China; [2]Institute of Radiation Oncology, Union Hospital, Tongji Medical College, Huazhong University of Science and Technology, Wuhan, Hubei 430022, P.R. China; [3]Cancer Center, Hubei Key Laboratory of Precision Radiation Oncology, Institute of Radiation Oncology, Union Hospital, Tongji Medical College, Huazhong University of Science and Technology, Wuhan, Hubei 430022, P.R. China; [4]Department of Cardiovascular Surgery, Union Hospital, Tongji Medical College, Huazhong University of Science and Technology, Wuhan, Hubei 430022, P.R. China; [5]Department of Orthopedics, Union Hospital, Tongji Medical College, Huazhong University of Science and Technology, Wuhan, Hubei 430022, P.R. China; [6]Department of Hepatobiliary Surgery, Union Hospital, Tongji Medical College, Huazhong University of Science and Technology, Wuhan, Hubei 430022, P.R. China

Received October 7, 2025; Accepted February 24, 2026

DOI: 10.3892/mmr.2026.13866

Abstract. Lung cancer is an aggressive malignancy associated with a rapid progression and poor prognosis, for which immunotherapy only exhibits modest efficacy in most patients. In lung cancer, high lactate is associated with a low immunotherapy response and shortened survival; however, causal lactylation-related genes remain to be elucidated. In the present study, candidate genes were screened using Mendelian randomization (MR) analysis, with expression quantitative trait loci data and genome-wide association study summary statistics used as analytical resources. A total of 46 lactylation-related genes were included in the MR analysis, and multiple testing correction was performed using the false discovery rate (FDR) and Bonferroni methods to control the false-positive risk. MR identified three core genes [platelet-type phosphofructokinase; SWI/SNF related, matrix associated, actin dependent regulator of chromatin, subfamily a, member 4; and stathmin 1 (*STMN1*)]. Among these genes, only *STMN1* was significantly associated with increased lung cancer risk (inverse variance weighting original P=0.005, FDR-corrected P=0.014995, Bonferroni-corrected P=0.014995, odds ratio=1.741, 95% confidence interval: 1.182-2.564), with robust results confirmed by heterogeneity/pleiotropy/sensitivity analyses. Subsequently, transcriptomic analysis was conducted to assess *STMN1* expression in lung cancer tissues and its association with patient survival. *In vitro* (cell proliferation, migration, invasion and apoptosis assays) and *in vivo* experiments (murine tumor models) were also conducted to explore the function of *STMN1*. *STMN1* exhibited upregulation in lung cancer tissues, and was associated with a shorter survival, reduced antitumor immune cell infiltration and an immunosuppressive tumor microenvironment (TME) phenotype. *STMN1* knockdown inhibited lung cancer malignancy both *in vitro* and *in vivo*, and modulated key markers, whereas its overexpression exhibited the opposite effects. Additionally, *STMN1* promoted global histone lactylation and histone H3 lysine 18 lactylation in lung cancer cells, establishing a direct functional link between *STMN1* and the lactylation pathway. In conclusion, *STMN1* is a lactylation-related causal oncogene in lung cancer, driving progression via malignant phenotypes, and its high expression is associated with an immunosuppressive TME that may synergistically facilitate tumor progression. Therefore, *STMN1* may be considered a novel target for lung cancer therapy.

Correspondence to: Professor Qiuyue Zhang, Cancer Center, Union Hospital, Tongji Medical College, Huazhong University of Science and Technology, 1277 Jiefang Avenue, Jianghan, Wuhan, Hubei 430022, P.R. China
E-mail: zhangqiuyuezqy@163.com

Professor Shaobo Hu, Department of Hepatobiliary Surgery, Union Hospital, Tongji Medical College, Huazhong University of Science and Technology, 1277 Jiefang Avenue, Jianghan, Wuhan, Hubei 430022, P.R. China
E-mail: hu_shaobo@hust.edu.cn

*Contributed equally

Key words: stathmin 1, Lung cancer, Mendelian randomization, lactylation, tumor microenvironment

Introduction

The incidence of lung cancer is increasing worldwide (1). Notably, lung cancer is strongly associated with tobacco exposure, and it is characterized by a high tumor mutational burden, rapid disease progression, high propensity for recurrence and metastasis, and poor overall survival (OS) (2,3). Immune checkpoint inhibitors (ICIs) target signaling pathways such as programmed cell death protein 1/programmed cell death

ligand 1 and cytotoxic T-lymphocyte-associated protein 4, and offer renewed optimism for lung cancer treatment (4); however, their immunotherapeutic efficacy remains suboptimal. This is primarily due to the complex tumor microenvironment (TME) of lung cancer, which is characterized by low immunogenicity and prominent immune evasion (5). Therefore, to overcome the current challenges in lung cancer treatment, in-depth investigations are required into the molecular pathogenesis of lung cancer and the identification of target genes with clinical translational potential.

Lactate is a crucial metabolite within the TME (6) and lactate metabolism, driven by the Warburg effect, is a major pathway that undergoes alterations in cancer (7). This metabolic alteration leads to the overproduction of lactate, even in the presence of sufficient oxygen; this boosts tumor cell proliferation and creates an immunosuppressive TME (8). Increased lactate levels hinder immune function by altering the pH of the TME, thereby impairing the activity of cytotoxic T lymphocytes and dendritic cells (9). Additionally, lactate acts as the substrate for histone lactylation, a novel post-translational modification that has far-reaching effects on gene regulation. Histone lactylation participates in immune evasion by altering gene expression in the immune cells within the TME (10). This leads to increased expression of genes that inhibit immune activity, thereby assisting tumors in evading immune surveillance (11,12). For example, LDH-mediated histone H3K18 lactylation upregulates Nur77 to drive immune escape in small cell lung cancer (13,14).

Traditional observational studies are susceptible to confounding factors and reverse causality, hindering the establishment of conclusive gene-disease connections (15). Mendelian randomization (MR) overcomes this issue by employing genetic variants as instrumental variables (IVs). This method takes advantage of the random inheritance of these variants at birth to enhance causal inference. It allows for efficient deduction of causal links between exposures (such as gene expression and protein levels) and disease outcomes (such as lung cancer incidence) at the population level, while markedly reducing biases (16,17). Recently, MR analyses that integrate data from protein quantitative trait loci and expression quantitative trait loci (eQTL) have successfully identified numerous potential therapeutic targets in prostate cancer (18) and breast cancer (19), providing a novel paradigm for precision oncology investigations.

Given the critical roles of lactate metabolism and histone lactylation in tumor progression and immune regulation, the current study employed the MR approach to screen for lactylation-related genes, which may have a causal relationship with lung cancer. The present study aimed to offer novel perspectives for the mechanistic research and therapeutic target exploration of lung cancer.

Materials and methods

Study design and data sources. The present study employed a two-sample MR method. The eQTL datasets of lactylation-related genes were used as exposure variables, and the genome-wide association study (GWAS) summary statistics of lung cancer were used as outcome variables. As described previously (20-23), a catalog of 46 lactylation-related genes was compiled.

eQTL exposure data. The eQTL exposure data were acquired from the IEU OpenGWAS Project (https://opengwas.io/), a global public database. Single nucleotide polymorphisms (SNPs) exhibiting a strong association with the expression of the 46 lactylation-related genes ($P<5x10^{-8}$) were selected as IVs. To avoid weak instrument bias, only SNPs with an F-statistic >10 were included as IVs, ensuring a strong association between the IVs and gene expression.

Lung cancer outcome data. The lung cancer outcome data were sourced from the Finnish database (finngen_R12_C3_lung cancer_EXALLC; https://r12.finngen.fi/pheno/C3_lung_cancer_EXALLC), which included 909 lung cancer cases and 3,788,794 healthy controls. The GWAS summary statistics in this database contained ~21,325,071 SNPs.

MR analysis. The MR analyses were performed using R software (version 4.4.2; https://cran.r-project.org/bin/windows/base/old/4.4.2/) packages 'TwoSampleMR' (version 0.5.6; https://CRAN.R-project.org/package=TwoSampleMR), 'ieugwasr' (version 0.1.7; https://CRAN.R-project.org/package=ieugwasr) and 'MRInstruments' (version 0.4.0; https://CRAN.R-project.org/package=MRInstruments). IV selection was conducted by retaining SNPs strongly associated with lactylation-related gene expression ($P<5x10^{-8}$) and with an F-statistic>10 to avoid weak instrument bias; SNPs were then clumped to remove linkage disequilibrium (LD) using a threshold of $r<0.001$ and a window size of 1Mb to ensure independence. The processed eQTL data were used as the exposure dataset, and the lung cancer GWAS summary statistics were used as the outcome dataset. Prior to analysis, allele harmonization was performed to ensure consistency of allele orientation and effect direction between exposure and outcome datasets. Strand-ambiguous SNPs and those with conflicting effect directions were excluded. The specific methods employed in the present study included inverse variance weighting (IVW), MR Egger, weighted median, simple mode and weighted mode. For each gene, the causal impact size (β), P-value, standard error, 95% confidence interval (95% CI) and odds ratio were recorded. Subsequently, The heterogeneity and pleiotropy of the odds ratio were calculated using Cochran's Q test (for heterogeneity) and the MR Egger intercept test (for horizontal pleiotropy), followed by multivariate sensitivity analyses including leave-one-out validation and MR-PRESSO outlier detection. The reliability of the MR findings was confirmed using scatter diagrams, forest plots and leave-one-out sensitivity analysis. Funnel plots were generated to assess potential publication bias and the presence of outliers. The screening criteria for core causal genes were set as $P<0.05$ in the IVW method and uniform OR direction trends across all five analytical approaches.

Multiple testing correction. The multiple testing correction protocol was performed as follows: First, the IVW P-values of all lactylation-related genes were extracted from the MR analysis results to construct a raw P-value dataset. Second, the 'p.adjust' function in R software (version 4.4.2; r-project.org/) was used to implement false discovery rate (FDR) and Bonferroni corrections, with the correction base set as the number of effectively analyzed candidate genes; the FDR

correction threshold was defined as 0.05 to balance false-positive and false-negative risks, whereas the Bonferroni correction threshold was set to 0.05 divided by the number of effectively analyzed genes as a strict verification standard. Finally, genes with corrected P-values below the corresponding thresholds were identified as significantly associated genes, and the screening criteria for core causal genes were updated to: IVW method P<0.05, consistent OR directions across all five MR analytical methods, and statistical significance after at least one multiple testing correction.

Transcriptomic analysis. The transcriptomic data, including five Gene Expression Omnibus (GEO) datasets, among which GSE6044 included nine lung cancer tissues and 5 normal lung tissues, GSE11969 included 9 lung cancer tissues and 5 normal lung tissues, GSE40275 included 15 lung cancer tissues and 41 normal lung tissues, and GSE43346 included 23 lung cancer tissues and 42 normal lung tissues. (ncbi.nlm.nih.gov/geo/query/acc.cgi?acc=GSE6044; ncbi.nlm.nih.gov/geo/query/acc.cgi?acc=GSE11969; ncbi.nlm.nih.gov/geo/query/acc.cgi?acc=GSE40275; ncbi.nlm.nih.gov/geo/query/acc.cgi?acc=GSE43346). Expression data from three independent studies: George *et al* (24), Cai *et al* (25) and Liu *et al* (26) were also included.

Analysis of expression and survival. RNA sequencing data from the GEO datasets underwent differential expression profiling using the R software package 'limma' (version 3.58.1; https://www.bioconductor.org/packages/release/bioc/html/limma.html). Log_2 fold change (log_2FC) and adjusted P-value (P.adj) for Stathmin1 (*STMN1*) were calculated in tumor vs. normal tissues derived from healthy individuals. The differential expression profiles were visualized using box plots. Kaplan-Meier survival analysis, paired with the log-rank test, was used to explore the relationship between *STMN1* expression and OS, with all computations conducted in the 'survival' R package (version 3.5-8; https://CRAN.R-project.org/package=survival) and survival curves visualized for publication using 'survminer' (version 0.4.9; https://CRAN.R-project.org/package=survminer). The findings from multivariate Cox proportional hazards regression analysis were illustrated using a forest plot, which was generated with the 'forestplot' R package (version 2.0.5; CRAN.R-project.org/package=forestplot).

Immune correlations. The 'MCPcounter' (Microenvironment Cell Populations counter) method was used to measure the infiltration abundance of 10 immune cell subsets (version 1.0.0; https://github.com/ebecht/MCPcounter). All analyses were conducted using the George *et al* (24) dataset. Samples were dichotomized into the low and high *STMN1* expression group by taking the median *STMN1* expression level as the cut-off value. The abundances of major immune cell infiltration were further characterized using the Cell-type Identification By Estimating Relative Subsets of RNA Transcripts ('CIBERSORT' R package, version 1.0; cibersort.stanford.edu/) (27), MCPcounter (28), Estimation of Proportions of Immune and Cancer cells (EPIC) ('EPIC' R package, version 1.1.0; https://github.com/GfellerLab/EPIC) (29), Quantitative Transcriptomics for Immune cell Quantification (quanTIseq) ('quanTIseq' R package, version 2.1.0; https://icbi-lab.github.io/quanTIseq/) (30) and xCell algorithms ('xCell' R package, version 1.1; https://xcell.ucsf.edu/) (31). Moreover, the expression patterns of immune checkpoint molecules were compared between the high and low *STMN1* expression groups. The ESTIMATE algorithm ('ESTIMATE' R package, version 1.0.13; https://CRAN.R-project.org/package=ESTIMATE) and Spearman's rank correlation analysis ('stats' R package, version 4.4.0; https://CRAN.R-project.org/package=stats) were applied to calculate the correlation coefficient (R) and significance (P-value) between *STMN1* expression and stromal score, immune score, estimate score and tumor purity.

Mutation data processing. The association between *STMN1* expression and lung cancer-related genomic alterations, including copy number variations (CNVs) and somatic single-nucleotide variants/indels, was evaluated using Spearman's rank correlation analysis and OR analysis. CNVs were obtained from cBioPortal (cbioportal.org/) and classified into amplification and homozygous deletion types. Somatic mutation data, including SNPs, and insertions and deletions, were obtained from the UCSC genome browser (https://genome.ucsc.edu/). The R software package 'maftools' was used for the data integration and analysis (version 2.14.0; bioconductor.org/packages/release/bioc/html/maftools.html), and the R software packages 'read.maf' and 'oncoplot' (integrated in maftools version 2.14.0) were used for file import facilitation and generating waterfall plot visualizations. The enrichment of mutated genes in patients with lung cancer and high or low *STMN1* expression in oncogenic signaling pathways was also analyzed. All analyses were conducted using the George *et al* (24) dataset. Samples were dichotomized into the low *STMN1* expression group and high *STMN1* expression group by taking the median *STMN1* expression level (9.477354) as the cut-off value. The Drug-Gene Interaction database (DGIdb) (32) was used to generate a hypothesis on mutant gene druggability and match the gene lists to drug-gene interactions.

Functional enrichment and pathway analysis. The STMN1-associated proteins with differential expression were identified, and their expression patterns were visualized using volcano plots and heatmaps. A protein-protein interaction (PPI) network was built using Cytoscape (version 3.10.4; cytoscape.org/Cytoscape) and the hub proteins within this network were identified using the cytoHubba plugin. All analyses were conducted using the Liu *et al* (26) dataset. Additionally, the top 20 proteins co-expressed with STMN1 were selected for in-depth investigation. Enrichment analysis was conducted on these proteins to clarify the potential mechanisms underlying the role of STMN1 in lung cancer. Prior to this analysis, Pearson correlation analysis was used to filter *STMN1*-associated genes based on the criteria of a correlation coefficient >0.3 and P<0.05. Subsequently, over-representation analysis (ORA) was performed by leveraging datasets from Kyoto Encyclopedia of Genes and Genomes (KEGG; genome.jp/kegg/), Reactome (reactome.org/), WikiPathways (https://www.wikipathways.org/) and Gene Ontology (GO; geneontology.org/Gene Ontology),

with support from the R packages including 'clusterProfiler' (version 4.10.0; https://bioconductor.org/packages/clusterProfiler/), 'org.Hs.eg.db' (version 3.18.0; https://bioconductor.org/packages/org.Hs.eg.db/) and 'ReactomePA' (version 1.46.0; https://bioconductor.org/packages/ReactomePA/).

Cell lines and culture conditions. The RP1 cell line is a well-characterized immortalized lung cancer cell line established by immortalizing the primary lung cells isolated from $Rb^{L/L}/Trp53^{L/L}$ (Rb1 and Trp53 conditional double knockout) mice. Specifically, the cell line was derived from spontaneous lung cancer tumors induced by intranasal inhalation of adenovirus-mediated Cre recombinase in these knockout mice, which triggers specific deletion of Rb1 and Trp53 genes in lung tissues. Primary tumor cells were subsequently isolated from the induced lung cancer lesions and immortalized to generate the RP1 cell line, which has been verified to maintain stable proliferation and malignant phenotypes over continuous passages *in vitro*. This cell line was generously donated by the research group of Professor Hongbin Ji (Center for Excellence in Molecular Cell Science, Chinese Academy of Sciences, Shanghai, China) (33). The human lung cancer cell line DMS114, human lung sarcomatoid carcinoma cell line H196 and 293T cell line were purchased from The Cell Bank of Type Culture Collection of The Chinese Academy of Sciences. DMS114 and H196 were cultured in RPMI-1640 medium (Gibco; Thermo Fisher Scientific, Inc.) supplemented with 10% fetal bovine serum (FBS; Gibco; Thermo Fisher Scientific, Inc.), 100 IU/ml penicillin and 100 μg/ml streptomycin. 293T cells were cultured in Dulbecco's Modified Eagle Medium (Gibco; Thermo Fisher Scientific, Inc.) supplemented with 10% FBS, 100 IU/ml penicillin, and 100 μg/ml streptomycin. All of the cells were maintained in a humidified incubator at 37˚C with 5% CO_2 and were passaged every 2-3 days once they reached 80-90% confluence.

The cell lines were authenticated by short tandem repeat (STR) profiling, and were confirmed to match reference STR profiles in the American Type Culture Collection (atcc.org/), DSMZ (dsmz.de/), Japanese Collection of Research Bioresources (cellbank.nibio.go.jp/) and ExPASY/Cellosaurus databases (cellosaurus.org/), verifying their identity and ruling out cross-contamination.

Construction of stable cell lines. Briefly, 293T cells were seeded in 10-cm culture dishes at a density of $5x10^6$ cells/dish 24 h prior to transfection, ensuring cells reached 70-80% confluence. All lentiviral vectors (pLKO.1, pCDH/hygro, psPAX2, pMD2.G) were obtained from Addgene, Inc. Lentiviral packaging was performed using a third-generation packaging system.

For knockdown, short hairpin RNA (shRNA) sequences were inserted into the pLKO.1 lentiviral vector, and an empty vector was used as a negative control. Lentiviral packaging and infection were performed identically for both knockdown and overexpression constructs. For transfection, a total of 6 μg plasmid DNA was used at a ratio of lentiviral vector: psPAX2: pMD2.G=2:1:1. Transfection was performed using polyethylenimine (cat. no. 40820ES, Yeasen Biotech Co., Ltd.) at 37˚C in a 5% CO_2 incubator for 6 h. Lentiviral supernatants were collected at 48 h post-transfection and filtered through a 0.45 μm filter. RP1, DMS114 and H196 cells were infected with lentivirus at a multiplicity of infection of 10 for 24 h. The culture medium was replaced with fresh complete medium. Cells were cultured at 37˚C in a 5% CO_2 incubator for an additional 48 h before antibiotic selection. Stable knockdown cell lines were established by selection with 1 μg/ml puromycin for 2 weeks, and maintained in medium containing 0.5 μg/ml puromycin thereafter. The shRNA sequences are listed in Table I.

For overexpression, the human *STMN1* gene was amplified using PCR and then ligated with the digested pCDH/hygro lentiviral vector to construct a recombinant plasmid (*STMN1*-OE). For the negative control, an empty pCDH/hygro vector without the STMN1 insert was used to infect cells in parallel. The successful construction of the recombinant plasmid was then verified through transformation, single colony screening and Sanger sequencing. Subsequently, the recombinant plasmid was co-transfected with packaging plasmids into 293T cells for viral packaging, followed by the collection of lentivirus-containing supernatant. Ultimately, DMS114 and H196 cells were infected with the viral supernatant. Stable STMN1 overexpression cell lines were established by selection with 200 μg/ml hygromycin B for 10-14 days, and maintained in complete medium supplemented with 100 μg/ml hygromycin B.

Western blotting. Total proteins were isolated from cultured lung cancer cells (DMS114, H196, RP1) and mouse subcutaneous tumor tissue using radioimmunoprecipitation assay (RIPA) lysis buffer (supplemented with protease and phosphatase inhibitors). Histones were extracted employing the 0.2 mol/l H_2SO_4 method: Cell pellets were resuspended in histone extraction buffer [10 mmol/l HEPES (pH 7.9), 1.5 mmol/l $MgCl_2$, 10 mmol/l KCl, 0.5 mmol/l DTT] and incubated on ice for 30 min. 5 mol/l H_2SO_4 to achieve a final concentration of 0.2 mol/l, and the mixture was incubated at 4˚C overnight. Following centrifugation at 13,700 x g at 4˚C for 10 min, 100% trichloroacetic acid was added to the supernatant to achieve a final concentration of 20%, followed by precipitation at 4˚C for 2 h. The precipitate was collected and washed three times with cold acetone, lyophilized under vacuum and dissolved in histone lysis buffer [20 mmol/l Tris-HCl (pH 7.5), 7 mol/l urea, 2 mol/l thiourea, 4% CHAPS]. A total of 20 μg of total protein or 1 μg of histone protein were loaded per lane and separated by 12% SDS-PAGE gels. The proteins were then transferred to PVDF membranes, which were blocked with 5% skimmed milk for 60 min at room temperature to minimize non-specific antibody adsorption. For immunodetection, the blocked membranes were incubated with primary antibodies at 4˚C for 16 h, followed by incubation with HRP-linked secondary antibodies for 1 h at room temperature. The protein bands were visualized using the Pierce ECL Western blotting Substrate (Thermo Fisher Scientific, Inc.), and the band optical density was analyzed using ImageJ software (version 1.53t; National Institutes of Health). The primary antibodies used in the present study were as follows: Anti-STMN1 (1:1,000; cat. no. TB2777;), anti-Bcl-2 (1:1,000; cat. no. T40056), anti-Vimentin (1:1,000; cat. no. T55134), anti-GAPDH (1:10,000; cat. no. P60037) (all from Abmart Pharmaceutical Technology Co., Ltd.), global histone lysine

Table I. shRNA sequences.

shRNA	Targeting portion, 5'→3'
shNC	CCTAAGGTTAAGTCGCCCTCG
Mouse	
STMN1-sh1	GCAGAAGAAAGACGCAAGTCT
STMN1-sh2	AGAAGGACAAGCACGTGGAAG
Human	
STMN1-sh1	CTGGAGGAAATTCAGAAGAAA
STMN1-sh2	GAGCACGAGAAAGAAGTGCTT

NC, negative control; sh, short hairpin; STMN1, stathmin 1.

lactylation (Pan Kla) (1:1,000; cat. no. 1401), histone H3 lysine 18 lactylation (H3K18la) (1:1,000; cat. no. 1427RM) (both from PTM BIO LLC) and Histone H3 (1:1,000; cat. no. 17168-1-AP; Proteintech Group, Inc.). HRP-linked secondary antibodies used were horseradish peroxidase-conjugated goat anti-rabbit IgG (1:5,000; cat. no. SA00001-2; Proteintech Group, Inc.) and horseradish peroxidase-conjugated goat anti-mouse IgG (1:5,000; cat. no. SA00001-1; Proteintech Group, Inc.).

Co-immunoprecipitation (co-IP). For IP, 500 μg total protein (200 μl of cell lysate) extracted from human lung cancer DMS114 and H196 was diluted to 500 μl with IP lysis buffer [20 mmol/l Tris-HCl (pH 7.5), 150 mmol/l NaCl, 1% Nonidet P-40 (NP-40), 1 mmol/l EDTA, supplemented with protease and phosphatase inhibitors]. The protein solution was pre-cleared with 20 μl protein A/G agarose beads (Santa Cruz Biotechnology, Inc.) at 4˚C for 1 h to reduce non-specific binding. After centrifugation at 118,000 x g at 4˚C for 10 min, the supernatant was incubated with 2 μg anti-STMN1 antibody (cat. no. TB2777; Abmart Pharmaceutical Technology Co., Ltd.) or 2 μg normal IgG (cat. no. 30000-0-AP; Proteintech Group, Inc.) as a negative control at 4˚C overnight with gentle rotation. Subsequently, 30 μl protein A/G agarose beads were added and incubated for another 4 h at 4˚C. The beads were washed four times with IP wash buffer [20 mmol/l Tris-HCl (pH 7.5), 300 mmol/l NaCl, 1% NP-40, 1 mmol/l EDTA]. After a final centrifugation at 78,400 x g at 4˚C for 3 min, immune complexes were eluted by boiling with 2X SDS loading buffer for 10 min. The eluted proteins were then subjected to SDS-PAGE and western blotting as aforementioned.

Cell viability and colony formation assays. Cell viability was evaluated using the Cell Counting Kit-8 (CCK-8; cat. no. B34302; Selleck Chemicals). Briefly, DMS114 and H196 cells were seeded onto 96-well culture plates at a density of ~3,000 cells/well. After adhering to the plate, the cells were subjected to the required treatment: Continuous culture for an additional 48 h in a standard 37˚C, 5% CO_2 incubator under normal growth conditions. The CCK-8 reagent was then added according to the manufacturer's instructions at 37˚C with 5% CO_2 for 2 h. To assess cell viability, the absorbance value was measured at 450 nm wavelength using a microplate reader.

For the colony formation assay, DMS114 and H196 cells were seeded onto 6-well plates at a density of ~500 cells/well and maintained in culture for 14 days to allow colony formation. After 14 days, the cells were then washed with phosphate-buffered saline (PBS) to eliminate leftover medium. They were subsequently fixed in 4% paraformaldehyde (PFA) at room temperature for 15 min and stained with 0.1% crystal violet solution at room temperature for 20 min to make colonies visible. The cells were then re-rinsed with PBS to eliminate excess stain and finally air-dried at room temperature for subsequent colony counting and analysis. Colonies were defined as cell clusters containing >50 cells, and counting was performed using ImageJ software (version 1.53t; National Institutes of Health) in a blinded manner.

Wound-healing assay. DMS114 and H196 cells with stable *STMN1*-knockdown (*STMN1*-sh) or overexpression (*STMN1*-OE) were seeded onto 6-well plates. Subsequently, 2 ml culture medium (supplemented with 10% FBS) was added to each well, and the cells were cultured for 24 h to allow adherence and initial growth. Upon reaching 95-100% cell confluence, vertical scratches were made on the confluent cell monolayer using a sterile 200-μl pipette tip. The scratched cells and cell debris were gently rinsed off with PBS to ensure a clear scratch area. The plates were then refreshed with 2 ml serum-free media to minimize the interference of cell proliferation, and the cells were incubated for another 24 h. Cell migration was monitored by capturing images of the scratch areas at 0, 12 and 24 h under a light microscope (x4 magnification). For each experimental group, three random fields were imaged to ensure data reproducibility. The migration rate was calculated using the following formula: Migration rate (%)=[(Scratch width at 0 h-Scratch width at each time point)/Scratch width at 0 h] x100.

Flow cytometric analysis. DMS114 and H196 cells were collected by centrifugation at 300 x g at 4˚C for 5 min, after which, the supernatant was discarded and the pellet was washed with 1 ml PBS. The cells were then centrifuged again at 300 x g at 4˚C for 5 min and the supernatant was discarded. The cell pellet was resuspended in 300 μl Stain Buffer (cat. no. 420201; Biolegend, Inc.), and PI-PE (cat. no. HY-D0815; MedChemExpress) and Annexin V-FITC (cat. no. 640949; Biolegend, Inc.) were added, at 4˚C in the dark for 15 min. Cell apoptosis was detected using a FACSCalibur flow cytometer (BD Biosciences). Data were analyzed using FlowJo software (version 10.8.1, BD Biosciences). Early apoptosis and late apoptosis were combined, and the total apoptosis rate was calculated using the following formula: Total apoptosis rate (%)=early apoptotic cells (%) + late apoptotic cells (%).

Transwell migration and invasion cell assays. Cell migration and invasion were evaluated using the Transwell assays (0.4-μm pore-size inserts in 12-well plates). For the cell migration assay, ~3x10^4 DMS114 or H196 cells were suspended in 200 μl serum-free medium. This cell suspension was seeded into the upper chambers of Transwell inserts, whereas 600 μl medium supplemented with 10% FBS was added to the lower chambers as a chemoattractant. After incubating the cells at 37˚C for 48 h, the non-migrated cells were removed

from the upper surface of the inserts using cotton swabs. The migrated cells adhering to the lower surface were fixed in 4% PFA for 20 min and then stained with 0.1% crystal violet for 20 min at room temperature, followed by rinsing with PBS. Images of the cells were captured under a light microscope at x10 magnification across three random fields, followed by cell counting.

For the cell invasion assay, the insert chambers were pre-coated with 50 μl Matrigel (diluted to 1:8 in ice-cold serum-free culture medium) at 37˚C for 60 min to construct a matrix barrier layer. The subsequent protocol was identical to that described for the migration assay.

Subcutaneous tumor model. 6-8-week-old male C57BL/6 mice (weight, 18~22 g) were purchased from the Laboratory Animal Center of Huazhong University of Science and Technology (Wuhan, China). A total of 15 mice were included All mice were housed at a temperature of 22±2˚C, with a relative humidity of 50-60%, a 12 h light/12 h dark cycle, and free access to standard chow and water. In order to establish subcutaneous tumors, the stably transduced RP1 cells (transduced with NC, *STMN1*-sh1 and *STMN1*-sh2) were respectively inoculated into the right axilla (~1x10^6 cells in 100 μl PBS/mouse, n=5/group). Tumor dimensions were recorded every 4 days for a total of 24 days. Tumor volume was calculated using the following formula: Tumor volume=1/2 x length x $width^2$. Humane endpoints were set as follows: i) tumor volume exceeding 2,000 mm^3; ii) >20% body weight loss; iii) severe signs of distress or impaired mobility. No mice met these endpoints On day 24, the mice were euthanized by cervical dislocation. Death was confirmed by two indicators: i) Complete cessation of thoracic movement and breathing for ≥1 min; and ii) absence of hindlimb withdrawal reflex when gently pinched with forceps. After confirming death, the tumor tissues were dissected, weighed and processed: Tissues were fixed in 4% PFA) at room temperature for 24 h, followed by paraffin embedding and sectioning at a thickness of 4 μm. Some tissue were lysed with RIPA lysis buffer (supplemented with protease and phosphatase inhibitors) for protein extraction and western blotting.

Hematoxylin and eosin (H&E) staining. The paraffin-embedded sections of subcutaneous tumor tissues were prepared. After gradient deparaffinization with xylene and rehydration with ethanol at room temperature, the sections were stained with hematoxylin for 10 sec at room temperature. Subsequently, the tissue sections were differentiated in 1% hydrochloric acid-ethanol at room temperature for 20 sec, blued in 0.5% ammonia water for 2 min and counterstained with eosin for 3 min at room temperature. The tissue sections were then dehydrated with gradient ethanol, cleared with xylene and mounted using neutral balsam at room temperature. Images were captured using a light microscope (Olympus BX53, Olympus Corporation).

Immunofluorescence staining. The paraffin-embedded subcutaneous tumor tissue sections were deparaffinized with xylene, rehydrated with a graded series of ethanol and subjected to antigen retrieval using citrate buffer (pH 6.0) at 95˚C for 15 min. The sections were then permeabilized with 0.2% Triton X-100 at room temperature for 10 min and blocked with 5% bovine serum albumin (BSA, cat. no. A1933, Sigma-Aldrich; Merck KGaA) at room temperature for 1 h. Subsequently, the sections were incubated with a primary antibody against Vimentin (cat. no. T55134; Abmart Pharmaceutical Technology Co., Ltd.) at a dilution of 1:200 at 4˚C overnight, followed by incubation with Cy3-conjugated goat anti-rabbit IgG (cat. no. GB21303; Wuhan Servicebio Technology Co., Ltd.) at a dilution of 1:400 for 1 h at room temperature. The cell nuclei were counterstained with DAPI at room temperature for 5 min. Images of the cells were captured under a fluorescence microscope, and the mean fluorescence intensity was analyzed and semi-quantified using ImageJ software (version 1.53t; National Institutes of Health).

Immunohistochemistry. The paraffin-embedded subcutaneous tumor tissue sections were deparaffinized with xylene, rehydrated with a graded series of ethanol. Antigen retrieval was performed using citrate buffer (pH 6.0) under high-pressure at 121˚C for 15 min to restore antigen epitopes. To eliminate endogenous peroxidase interference, the prepared sections were incubated with 3% hydrogen peroxide (H_2O_2) at room temperature for 10 min, and to block the non-specific antibody binding, they were treated with 5% BSA at room temperature for 60 min. The sections were then incubated with primary antibodies, including anti-Ki67 (cat. no. TW0001; Abmart Pharmaceutical Technology Co., Ltd.), anti-Caspase-3 (cat. no. 19677-1-AP; Proteintech Group, Inc.) and anti-Cleaved-Caspase-3 (C-Caspase-3; cat. no. AF7022; Affinity Biosciences) overnight at 4˚C. The next day, the sections were incubated with HRP-conjugated secondary antibodies (cat. no. SA00001-2; Proteintech Group, Inc.) at room temperature for 1 h. DAB chromogen (cat. no. DA1010; Beijing Solarbio Science & Technology Co., Ltd.) was used for visualization of protein expression with subsequent counterstaining with hematoxylin at room temperature for 10 sec. Under an optical microscope, three random high-power fields (x40 magnification) were assessed for each section. Positive cells were semi-quantified using Image-Pro Plus 6.0 software (Media Cybernetics, Inc.). The percentage of positive cells was calculated using the following formula: Positive cells (%)=[(Number of positive cells in each field/Total number of cells in each field)] x100, to assess protein expression levels. Integrated optical density (IOD) of positive staining was quantified using Image-Pro Plus 6.0 software (Media Cybernetics, Inc.). IOD represents the total optical density of positively stained areas, reflecting the overall expression level of the target protein. For C-Caspase-3, the IOD value was normalized to the IOD of total Caspase-3 to indicate the level of apoptotic activation.

TUNEL staining. Paraffin-embedded tumor tissue sections were deparaffinized in xylene and rehydrated through a graded ethanol series. Following antigen retrieval using proteinase K (20 μg/ml) for 20 min at 37˚C, the sections were incubated with the TUNEL reaction mixture at 37˚C for 60 min in the dark, according to the manufacturer's instructions (cat. no. C1088; Beyotime Biotechnology). Subsequently, the sections were mounted with an anti-fade mounting medium containing DAPI to visualize cell nuclei. Images were captured using

a fluorescence microscope equipped with appropriate filter sets for FITC and DAPI detection (Olympus BX53, Olympus Corporation, Tokyo, Japan). To ensure representative quantification, at least 3 randomly selected non-overlapping fields of view per section were observed. The apoptotic index was calculated as the ratio of TUNEL-positive cells (green fluorescence) to the total number of cells (blue fluorescence).

Cell lactate concentration measurement. Cellular lactate concentrations were measured using Lactate Colorimetric Assay Kit (cat. no. K607-100, BioVision, Inc., according to the manufacturer's instructions. DMS114 and H196 cells with stable *STMN1* knockdown or overexpression were seeded in 6-well plates at a density of $1x10^6$ cells/well and cultured for 48 h. After washing twice with ice-cold PBS, cells were lysed in lactate assay buffer and centrifuged at 12,000 x g for 10 min at 4˚C to remove cell debris. The supernatant was collected and incubated with the lactate detection reagent mix at 37˚C for 30 min in the dark. The absorbance was measured at 570 nm using a microplate reader, and lactate concentrations were calculated based on a standard curve generated with known lactate concentrations.

Statistical analysis. Pearson correlation coefficient was used to assess linear associations between *STMN1* expression and continuous variables with approximately normal distributions, such as the expression levels of co-expressed genes. Spearman's rank correlation coefficient was applied to evaluate non-linear or non-normally distributed relationships, including those between *STMN1* expression and immune cell infiltration scores, stromal/immune/ESTIMATE scores, tumor purity and genomic alteration frequencies. ORA was utilized for functional enrichment assessments. For the *in vitro* and *in vivo* experimental data, the results are presented as the mean ± standard deviation. Comparisons between two groups were performed using unpaired Student's t-test, whereas those among multiple groups were performed using one-way analysis of variance (ANOVA). When ANOVA results were significant, Bonferroni's multiple comparisons test was used for post-hoc analysis, comparing each experimental group with the control group. All *in vitro* experiments were performed with three biological replicates. $P<0.05$ was considered to indicate a statistically significant difference. For MR analyses, additional multiple testing corrections were performed using the FDR and Bonferroni methods, with FDR-corrected $P<0.05$ regarded as statistically significant.

Results

MR analysis of lactylation-associated genes and lung cancer. From the eQTL data of 46 lactylation-related genes, the IVs meeting strict quality control criteria for MR analysis were identified: 63 SNPs for the platelet-type phosphofructokinase (*PFKP*) gene (F-statistic=315.6), 8 SNPs for the SWI/SNF related, matrix associated, actin dependent regulator of chromatin, subfamily a, member 4 (*SMARCA4*) gene (F-statistic=92.7) and 7 SNPs for the *STMN1* gene (F-statistic=109.9). All of the IVs satisfied the strong instrument threshold (F>10). Following allele harmonization, no strand-ambiguous SNPs or SNPs with conflicting effect directions were detected. The detailed information on the finally included IVs is provided in Table II.

To investigate the causal relationships between these three core lactylation-related genes and lung cancer, MR analyses were conducted using multiple statistical approaches, including IVW, MR Egger, weighted median, simple mode and weighted mode. Among these methods, IVW served as the main model for causal inference ('I), and the detailed quantitative results of all five MR analytical methods for each gene are summarized in Table III. IVW analysis revealed that *PFKP* (OR=0.909, 95% CI: 0.845-0.979) and *SMARCA4* (OR=0.633, 95% CI: 0.409-0.979) were associated with a lower risk of lung cancer, whereas *STMN1* (OR=1.741, 95% CI: 1.182-2.564) was associated with an elevated risk.

Scatter diagrams were drawn to illustrate the detailed MR analyses results. The calculation of individual causal impacts demonstrated that increased SNP-mediated effects on *STMN1* expression were associated with elevated lung cancer risk (Fig. 1A). Conversely, enhanced SNP effects on *PFKP* and *SMARCA4* expression were linked to more pronounced protective effects against lung cancer (Fig. 1B and C). The effects of SNPs corresponding to each of the three core exposure factors (*STMN1*, *PFKP* and *SMARCA4*) on lung cancer risk were assessed by generating forest plots. Examining the effects of SNPs linked to each of the three key genes revealed consistent patterns across all analytical frameworks (Fig. 1D-F).

Multiple testing correction results. A total of three genes with valid MR results underwent multiple testing correction. *STMN1* was the only gene significantly associated with lung cancer risk in both correction methods. *PFKP* and *SMARCA4* were only significant after FDR correction, but not after Bonferroni correction (Table IV).

Sensitivity, pleiotropy and heterogeneity evaluations for MR outcomes. To enhance the reliability of the MR analyses findings, the IVs underwent rigorous screening standards, and all the samples were confined to a European ancestry cohort to reduce the risk of false-negative results and population stratification bias. The heterogeneity across SNPs linked to the three exposure factors (*STMN1*, *PFKP* and *SMARCA4*) was evaluated using Cochran's Q test and the MR Egger approach. The results showed no notable heterogeneity among the SNPs corresponding to the three genes, thus verifying the stability of the selected IVs (Table V).

Moreover, the MR Egger intercept test was conducted to detect the occurrence of horizontal pleiotropy. The respective intercept values were 0.012, 0.007 and 0.016 for *PFKP*, *SMARCA4* and *STMN1* genes, respectively, with no statistical significance. This result indicated that MR estimates were not biased by directional pleiotropy. The MR-PRESSO test did not identify any outliers (Table V).

A leave-one-out sensitivity assessment was additionally performed to evaluate the impact of individual SNPs on the overall IVW estimate. Excluding a single SNP had a minimal effect on the overall causal estimate (Fig. 1G-I). In addition, funnel plots were symmetric (Fig. 1J-L), indicating no significant publication bias or outlier interference. This observation confirmed that no individual SNP exerted a disproportionate

Table II. Basic information of instrumental variables selected from core lactylation-related genes.

Gene	No. of SNPs	P-value	Average F-statistic
PFKP	63	$1.00x10^{-200}$-$7.14x10^{-138}$	315.6
SMARCA4	8	$2.04x10^{-82}$-$8.55x10^{-13}$	92.7
STMN1	7	$7.51x10^{-77}$-$1.63x10^{-10}$	109.9

PFKP, platelet-type phosphofructokinase; *SMARCA4*, SWI/SNF related, matrix associated, actin dependent regulator of chromatin, subfamily a, member 4; SNPs, single nucleotide polymorphisms; *STMN1*, Stathmin 1.

Table III. Results of MR analyses for core lactylation-related genes and small-cell lung cancer risk.

A, *PFKP*

Analysis	No. of SNPs	β	SE	P-value	OR (95%CI)
MR Egger	63	-0.135	0.067	0.048	0.874 (0.766-0.996)
Weighted median	63	-0.071	0.057	0.209	0.931 (0.833-1.041)
IVW	63	-0.095	0.038	0.012	0.909 (0.845-0.979)
Simple mode	63	-0.110	0.083	0.191	0.896 (0.761-1.055)
Weighted mode	63	-0.087	0.061	0.159	0.916 (0.813-1.033)

B, *SMARCA4*

Analysis	No. of SNPs	β	SE	P-value	OR (95%CI)
MR Egger	8	-0.518	0.551	0.384	0.596 (0.202-1.754)
Weighted median	8	-0.514	0.265	0.053	0.598 (0.355-1.006)
IVW	8	-0.458	0.223	0.040	0.633 (0.409-0.979)
Simple mode	8	-0.711	0.442	0.152	0.491 (0.207-1.169)
Weighted mode	8	-0.551	0.288	0.098	0.576 (0.328-1.014)

C, *STMN1*

Analysis	No. of SNPs	β	SE	P-value	OR (95%CI)
MR Egger	7	0.414	0.453	0.402	1.513 (0.623-3.674)
Weighted median	7	0.419	0.242	0.084	1.520 (0.946-2.442)
IVW	7	0.555	0.198	0.005	1.741 (1.182-2.564)
Simple mode	7	0.782	0.370	0.079	2.185 (1.058-4.514)
Weighted mode	7	0.321	0.301	0.328	1.379 (0.764-2.489)

CI, confidence interval; IVW, inverse variance weighting; MR, Mendelian randomization; OR, odds ratio; *PFKP*, platelet-type phosphofructokinase; SE, standard error; *SMARCA4*, SWI/SNF related, matrix associated, actin dependent regulator of chromatin, subfamily a, member 4; SNPs, single nucleotide polymorphisms; *STMN1*, Stathmin 1.

influence on the outcomes, thus enhancing the credibility and stability of the MR results.

Among the three core lactylation-related genes identified by MR analysis, *STMN1* was the only gene that exhibited a significant causal association with increased lung cancer risk after both FDR and Bonferroni corrections, and its upregulation in lung cancer tissues was correlated with poor patient prognosis.

Expression, survival and functional enrichment analyses of STMN1. Expression analyses of the GEO datasets (GSE6044,

Table IV. Multiple testing correction summary.

Gene	P-value	P-FDR	P-bonferroni	Significance-FDR	Significance-bonferroni
PFKP	0.0118	0.0178	0.0355	TRUE	FALSE
SMARCA4	0.0397	0.0397	0.1190	TRUE	FALSE
STMN1	0.0050	0.0150	0.0150	TRUE	TRUE

FDR, false discovery rate; *PFKP*, platelet-type phosphofructokinase; *SMARCA4*, SWI/SNF-related, matrix associated, actin dependent regulator of chromatin, subfamily a, member 4; *STMN1*, Stathmin 1.

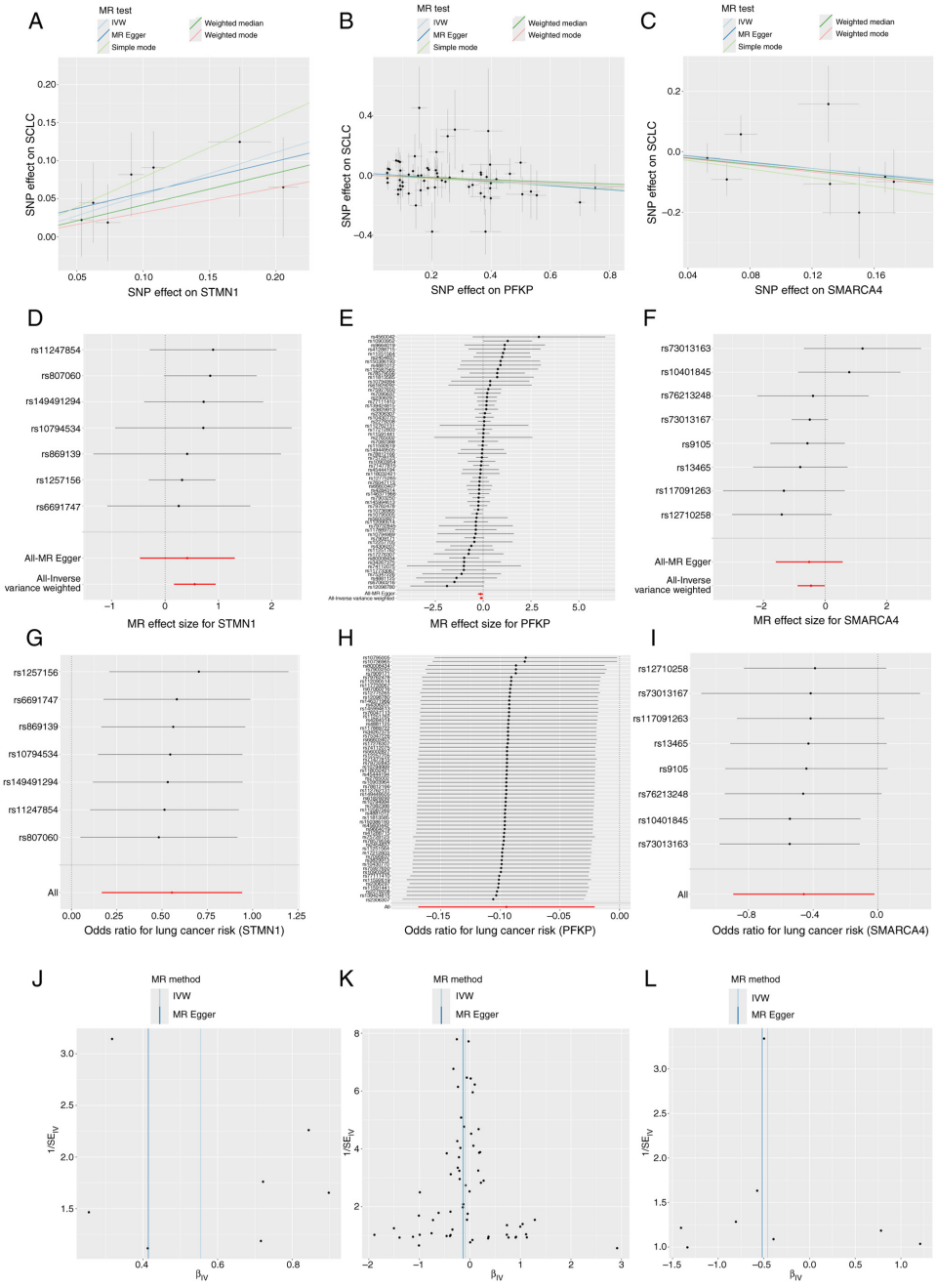

Figure 1. MR analysis and pleiotropy, heterogeneity and sensitivity analyses of lactylation-related genes and lung cancer. (A) Impact of SNPs on *STMN1*, (B) *PFKP* and (C) *SMARCA4* expression and lung cancer risk. (D) Effect sizes of SNPs related to *STMN1* on lung cancer risk. (E) Forest plot showing the effect sizes of SNPs related to *PFKP* and (F) *SMARCA4* on lung cancer risk. (G) Leave-one-out sensitivity analysis plot for *STMN1*. (H) Leave-one-out sensitivity analysis plot for *PFKP*. (I) Leave-one-out sensitivity analysis plot for *SMARCA4*. (J) Funnel plot for assessing publication bias and outliers related to *STMN1*, (K) *PFKP*. (L) Funnel plot for assessing publication bias and outliers related to *SMARCA4*. CI, confidence interval; IVW, inverse variance weighting; MR, Mendelian randomization; OR, odds ratio; *PFKP*, platelet-type phosphofructokinase; SE, standard error; *SMARCA4*, SWI/SNF related, matrix associated, actin dependent regulator of chromatin, subfamily a, member 4; SNPs, single nucleotide polymorphisms; *STMN1*, Stathmin 1.

Table V. Heterogeneity and pleiotropy tests for core lactylation-related genes.

	Heterogeneity test (IVW method)			Pleiotropy test (MR Egger intercept)		
Gene	Q value	df	P-value	Intercept	SE	P-value
PFKP	59.83	62	0.554	0.012	0.017	0.471
SMARCA4	7.49	7	0.380	0.007	0.062	0.908
STMN1	1.65	6	0.949	0.016	0.048	0.744

IVW, inverse variance weighting; MR, Mendelian randomization; *PFKP*, platelet-type phosphofructokinase; SE, standard error; *SMARCA4*, SWI/SNF related, matrix associated, actin dependent regulator of chromatin, subfamily a, member 4; *STMN1*, Stathmin 1.

GSE43346, GSE11969 and GSE40275) revealed that *STMN1* was significantly upregulated in lung cancer tissues compared with in normal tissues (Fig. 2A). Furthermore, the patients exhibiting high *STMN1* expression had a shorter OS time (Fig. 2B), and high *STMN1* expression was associated with a higher risk of poor prognosis (Fig. 2C).

Functional enrichment analyses were performed to investigate the biological roles of STMN1. KEGG pathway enrichment analysis (Fig. 2D) demonstrated significant enrichment in pathways, including 'spliceosome' and 'ATP-dependent chromatin remodeling'. Reactome enrichment analysis (Fig. 2E) highlighted its enrichment in processes, including 'processing of capped intron-containing pre-mRNA', 'mRNA splicing major pathway' and 'mRNA splicing'. WikiPathways enrichment analysis (Fig. 2F) revealed its role in the 'mRNA processing' pathway.

Immune correlations. Immune cell infiltration profiling revealed that the infiltration scores of B lineage cells, $CD4^+$ T cells, fibroblasts, monocytic lineage cells and neutrophils were significantly lower in the high *STMN1* expression group as compared with those in the low *STMN1* expression group (Fig. 3A). The correlation analysis of *STMN1* expression and immune checkpoint molecules further revealed an inverse association between *STMN1* and most immune checkpoint molecules (Fig. 3B), suggesting a potential role of STMN1 in modulating checkpoint-mediated immune suppression. In order to validate the association between *STMN1* and key antitumor immune cells, the infiltration abundances of $CD4^+$ and $CD8^+$ T cells and M1 macrophages were quantified using five independent algorithms (CIBERSORT, MCPcounter, EPIC, quanTIseq and xCell). All of the algorithms demonstrated a weak inverse correlation between *STMN1* expression and the infiltration of these three cell types (Fig. 3C-E), highlighting the association between *STMN1* and reduced antitumor immune cell infiltration. ESTIMATE algorithm-derived immune scores combined with Spearman's rank correlation analysis confirmed that high *STMN1* expression was weakly negatively correlated with the overall immune score (r=-0.276; Fig. 3F). These results indicated that *STMN1* high expression may be associated with the characteristics of an immunosuppressive TME in lung cancer, suggesting a potential role of *STMN1* in regulating TME immune status.

Genomic alteration analyses of STMN1. Waterfall plots visualized the genetic mutation patterns of lung cancer samples across *STMN1* expression subgroups. In the high *STMN1* expression group (Fig. 4A), all 35 lung cancer samples (100%) harbored genetic mutations. Moreover, 34 of 36 samples (94.44%) in the low *STMN1* expression group (Fig. 4B) exhibited genetic alterations, with mutation types comparable to those in the high *STMN1* expression subgroup. OR analysis was performed to quantify the association between *STMN1* expression and gene mutation status. Numerous genes, including *TRIM58*, *GCN1L1*, *KIAA1239*, *LRP1*, *SLITRK3*, *APOB*, *GPRC6A* and *TP53*, showed an OR of >1, indicating a higher mutation probability in the high *STMN1* expression group. On the other hand, genes such as *MYPN*, *COBL* and *LRFN5*, had an OR of <1, suggesting a lower mutation probability with high *STMN1* expression (Fig. 4C).

As compared with in the low *STMN1* expression group (Fig. 4E), the high *STMN1* expression group (Fig. 4D) was relatively highly enriched in the TP53 signaling pathway (94.12% vs. 83.78%), Hippo signaling pathway (79.41% vs. 72.97%), cell cycle (79.41% vs. 70.27%) and WNT signaling pathway (64.71% vs. 56.76%). By contrast, the enrichment levels of the RTK-RAS (76.47% vs. 78.38%) and NOTCH (76.47% vs. 75.68%) signaling pathways demonstrated no statistically significant difference between the two groups. The druggable categories in the lung cancer subgroups (high and low *STMN1* expression groups) were analyzed using the DGIdb. In the high *STMN1* subgroup, druggable categories included 'serine threonine kinase' (such as TTN), 'transporter' (such as RYR2) and TP53-related histone modification pathways, with 'druggable genome' involving *COL11A1* and *RB1* (Fig. 4F). The druggable categories in the low *STMN1* expression subgroup included 'serine threonine kinase' (such as TTN), TP53-related RNA-directed DNA polymerases, 'fibrinogen' (TNR) and 'drug resistance' (TP53), with 'druggable genome' involving *ABCA13* and *COL11A1* (Fig. 4G). Despite the overlapping core elements, gene composition in druggable categories was different, suggesting that *STMN1* expression may shape druggable target landscapes in lung cancer and guide subgroup-specific therapies.

Identification and functional analysis of proteins associated with STMN1 expression. To identify the proteins associated with varying *STMN1* expression levels, the protein expression patterns were visualized using volcano plots and heatmaps. These analyses revealed 452 differentially expressed proteins, including 72 upregulated and 380 downregulated proteins

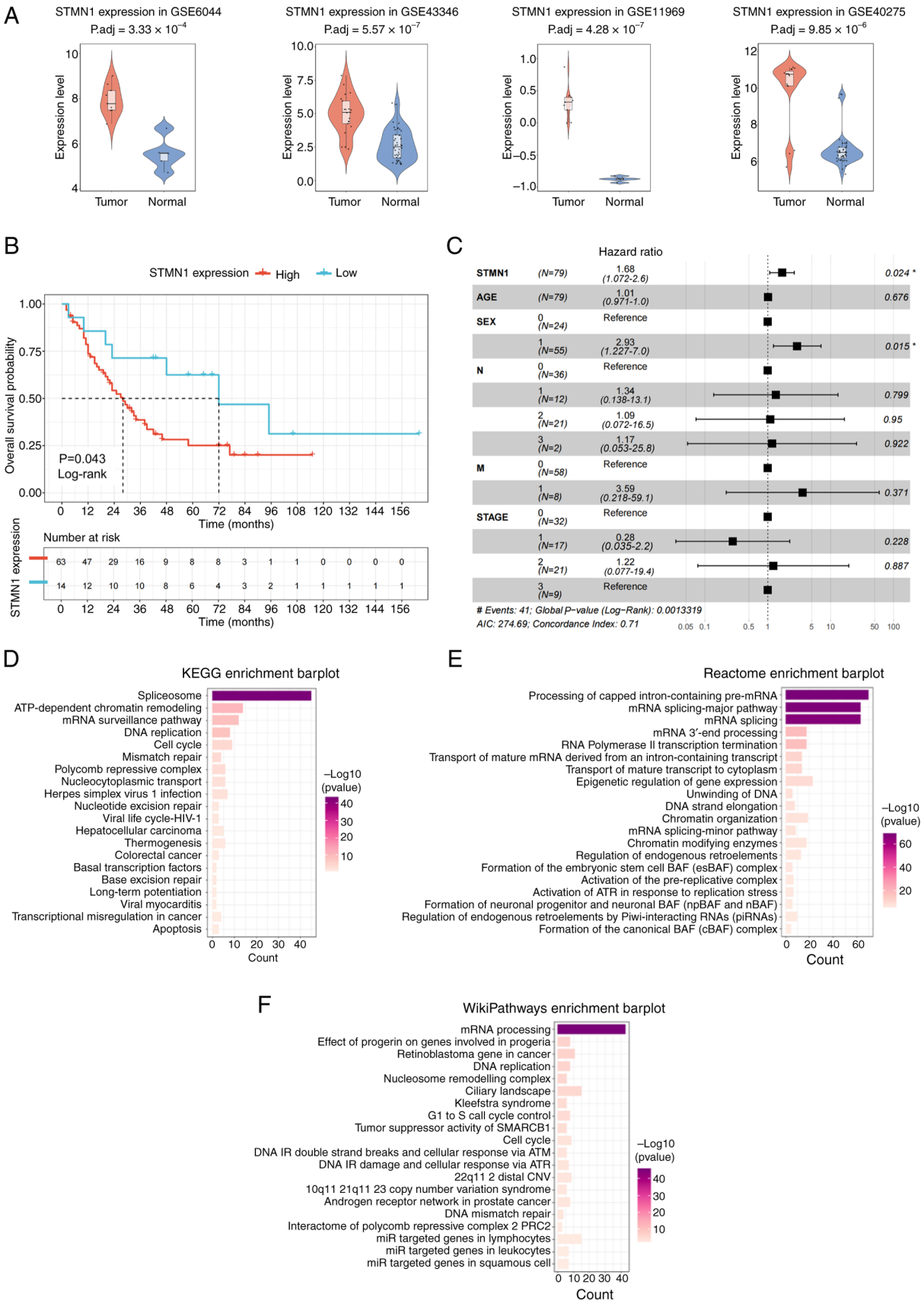

Figure 2. Prognostic and functional enrichment analyses of *STMN1* expression in lung cancer. (A) Box plots showing *STMN1* expression levels in lung cancer tissues and normal lung tissues across four Gene Expression Omnibus datasets (GSE6044, GSE43346, GSE11969 and GSE40275). (B) Kaplan-Meier survival curve analysis for the overall survival of patients with lung cancer based on *STMN1* expression (high *vs.* low). (C) Forest plot of multivariate Cox proportional hazards regression analysis, depicting the association between *STMN1* expression and the prognosis of patients with lung cancer. Bar plots of functional enrichment analyses. *P<0.05. (D) KEGG pathway enrichment, (E) Reactome pathway enrichment and (F) WikiPathways enrichment. The horizontal axis depicts the enriched gene count and the vertical axis depicts pathway names; the color gradient indicates-log10(P-value). KEGG, Kyoto Encyclopedia of Genes and Genomes; P.adj, adjusted P-value; *STMN1*, Stathmin 1.

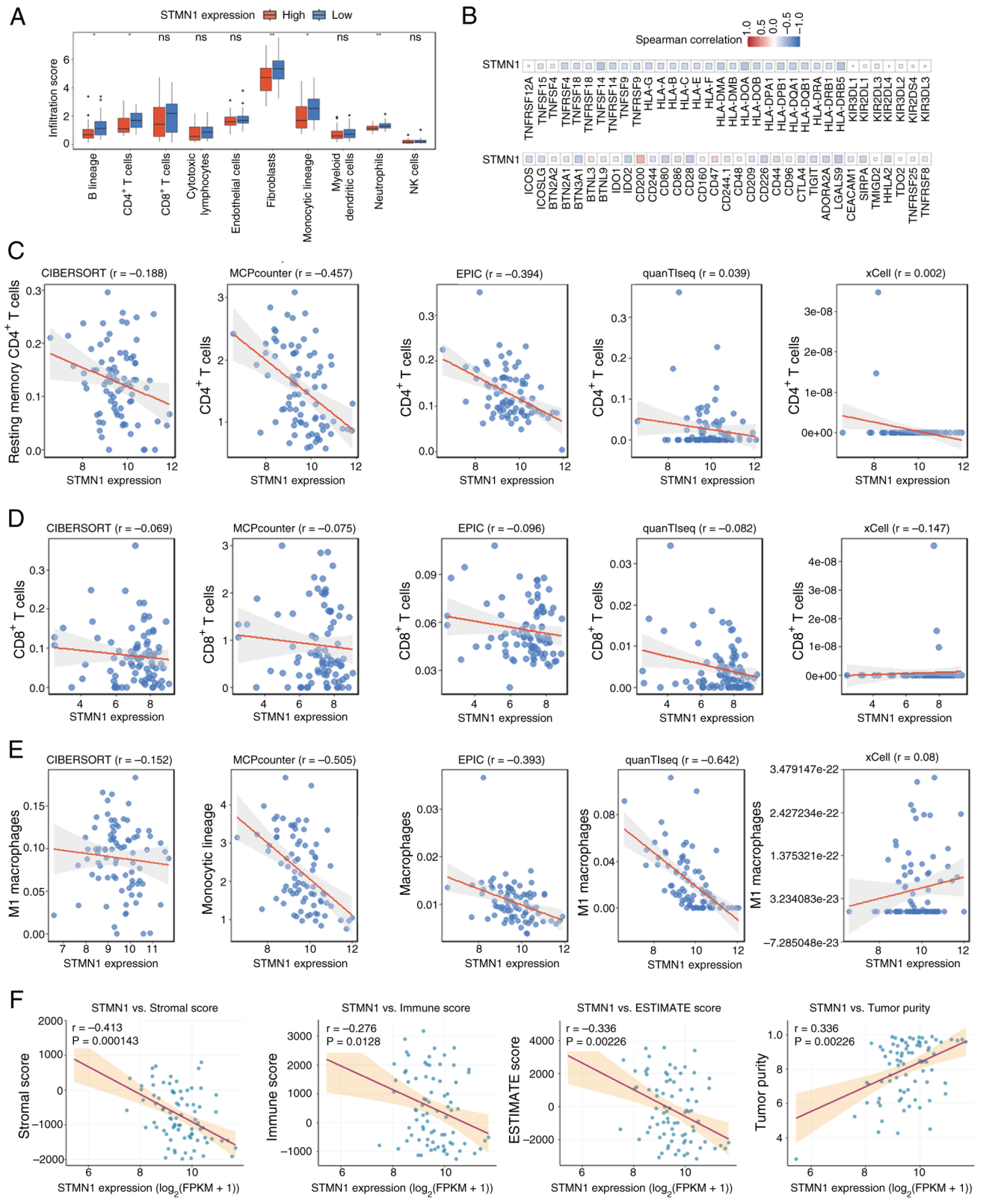

Figure 3. Correlation between *STMN1* expression and immune characteristics in lung cancer. (A) Bar plot comparing immune cell infiltration scores (quantified using the MCPcounter algorithm) between high and low *STMN1* expression groups. (B) Heatmap of Spearman correlation coefficients linking *STMN1* expression to immune checkpoint genes. The color gradient (blue to red) indicates the strength of correlation (negative to positive). (C) Association between *STMN1* expression level and infiltration abundance of $CD4^+$ T cells, quantified using five algorithms (CIBERSORT, MCPcounter, EPIC, quanTIseq and xCell). (D) Scatter diagram showing the association between *STMN1* expression level and infiltration abundance of $CD8^+$ T cells, quantified using five algorithms (CIBERSORT, MCPcounter, EPIC, quanTIseq and xCell). (E) Scatter diagram showing the association between *STMN1* expression level and infiltration abundance of M1 macrophages, quantified using five algorithms (CIBERSORT, MCPcounter, EPIC, quanTIseq and xCell). (F) Scatter diagrams of Spearman correlation between *STMN1* expression and Stromal Score, Immune Score, ESTIMATE Score and Tumor Purity (calculated using the ESTIMATE algorithm). Each plot includes the r- and P-values. *P<0.05, **P<0.01. CIBERSORT, Cell-type Identification By Estimating Relative Subsets of RNA Transcripts; EPIC, Estimation of Proportions of Immune and Cancer cells; MCPcounter, Microenvironment Cell Populations counter; quanTIseq, Quantitative Transcriptomics for Immune cell Quantification; *STMN1*, Stathmin 1.

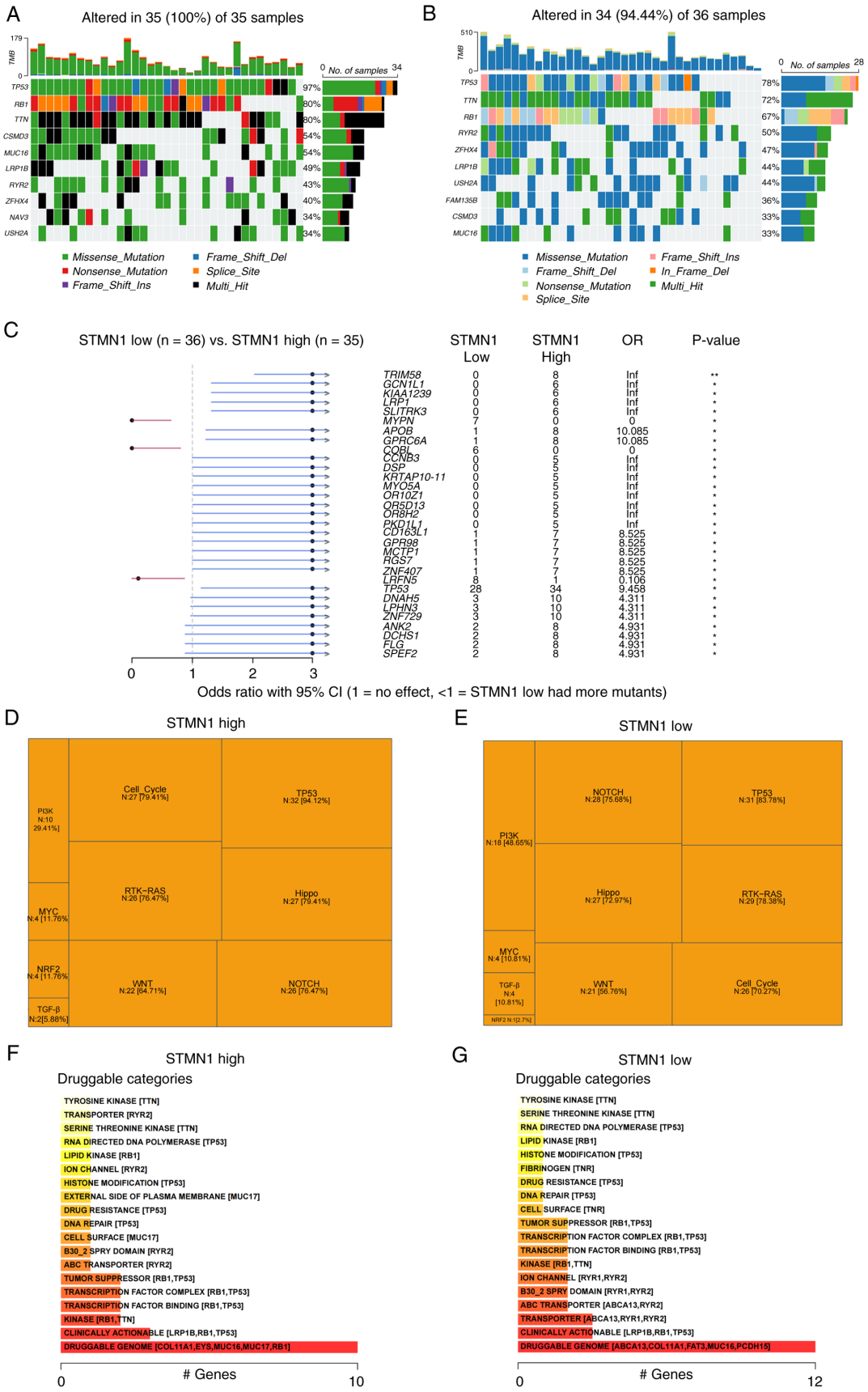

Figure 4. Genomic alterations and druggable target analysis based on *STMN1* expression in lung cancer. Waterfall plots showing genetic mutation patterns in (A) high and (B) low *STMN1* expression lung cancer subgroups. Distinct colors indicate various mutation categories. (C) Forest plot of OR analysis for gene mutation probability between *STMN1*-high and *STMN1*-low groups. Horizontal lines indicate 95% CIs and squares represent OR values. Treemaps showing the enrichment of key oncogenic signaling pathways in (D) high and (E) low STMN1 expression subgroups. Each rectangle represents a pathway, with its area proportional to the enrichment percentage; the sample number (N) and enrichment percentage of each pathway are annotated. Druggable target categories (analyzed using DGIdb) in (F) high and (G) low *STMN1* expression groups. *P<0.05, **P<0.01. CI, confidence interval; DGIdb, Drug-Gene Interaction Database; OR, odds ratio; *STMN1*, Stathmin 1.

(Fig. 5A and B). Next, a PPI network was drawn, and Cytoscape software was used to select hub proteins from the top 20 upregulated and top 20 downregulated proteins (Fig. 5C-F).

Subsequent GO enrichment analysis showed that *STMN1*-associated proteins were involved in the 'regulation of G_0 to G_1 cell cycle transition' and 'negative regulation of messenger RNA catabolic process' (Fig. 5G). These results indicated that *STMN1* could regulate cell cycle progression and maintain mRNA stability in lung cancer.

Effects of STMN1 on cell proliferation and migration in DMS114 and H196 cells. The effects of STMN1 expression were further assessed using cells transduced with NC, *STMN1*-sh1, *STMN1*-sh2, vector and *STMN1*-OE. Western blotting was performed to verify the efficiency of STMN1 knockdown and overexpression in DMS114 and H196 cells (Fig. 6A-D). In both cell lines, *STMN1*-sh1 and *STMN1*-sh2 significantly reduced STMN1 protein expression compared with the negative control group (Fig. 6A and C). Conversely, OE-*STMN1* markedly increased STMN1 protein levels relative to the vector control (Fig. 6B and D). These results confirmed the successful construction of stable *STMN1*-knockdown and -overexpression cell lines for subsequent functional assays. Subsequently, CCK-8 assays demonstrated that *STMN1* knockdown significantly suppressed cell proliferation in both DMS114 and H196 cells, whereas *STMN1*-OE transduction significantly accelerated cell proliferation (Fig. 6E-H). Moreover, wound healing assays showed that *STMN1* knockdown markedly impaired cell migration in both DMS114 and H196 cells, whereas its overexpression significantly accelerated cell migration (Fig. 6I-L).

Functional characterization of the effects of STMN1 on apoptosis, colony formation and cell invasion/migration. To characterize the functional role of *STMN1* in lung cancer, its effects on apoptosis, colony formation and invasion/migration were assessed in DMS114 and H196 cells. Flow cytometric analysis showed that *STMN1* knockdown significantly enhanced apoptosis in both cell lines. Total apoptosis rate was significantly higher in the *STMN1*-sh groups compared with the control group. By contrast, *STMN1* overexpression modestly decreased apoptosis, indicating that the pro-apoptotic effect of *STMN1* seems to be mainly achieved through its knockdown rather than overexpression (Fig. 7A-D). Colony formation assays revealed that *STMN1* knockdown markedly diminished colony-forming ability, which was evidenced by fewer and smaller colonies compared with that in the NC group (Fig. 7E and F). By contrast, *STMN1*-OE transduction significantly enhanced this capacity. Additionally, Transwell assays demonstrated that *STMN1* knockdown impaired invasive and migratory capacities (with fewer membrane-penetrating cells), whereas its overexpression significantly elevated these abilities (Fig. 7G-J).

STMN1 knockdown inhibits tumor growth in vivo. A murine shRNA model targeting *STMN1* was established to assess the *in vivo* effects of *STMN1*. As compared with in the NC group, both *STMN1*-sh1 and -sh2 groups exhibited reduced tumor volumes (Fig. 8A), decreased tumor weights (Fig. 8B) and slower tumor growth kinetics (Fig. 8C). The maximum tumor volume was 1,654 mm^3, corresponding to a maximum diameter of 15 mm. H&E staining and immunohistochemical analysis revealed that *STMN1* knockdown was associated with reduced expression of the proliferation marker Ki67, and elevated levels of the apoptosis marker C-Caspase-3/Caspase-3 in tumor tissues (Fig. 8D-F). Immunofluorescence staining demonstrated that Vimentin expression was reduced in the *STMN1*-sh1 and -sh2 groups, indicating impaired epithelial-mesenchymal transition (EMT) progression (Fig. 8G and H). The TUNEL assay further confirmed a significant increase in apoptotic cells in *STMN1*-knockdown tumors (Fig. 8I and J). Western blotting validated these findings, showing downregulated Vimentin and Bcl-2 (anti-apoptotic protein) expression levels in the *STMN1*-sh1 and -sh2 groups (Fig. 8K). These results were consistent with the enhanced apoptosis and suppressed EMT. *STMN1* knockdown efficiency was also confirmed in tumor tissues (Fig. 8K). Collectively, these results indicated that *STMN1* knockdown could induce tumor regression by suppressing cell proliferation, enhancing apoptosis and impairing EMT *in vivo*.

STMN1 promotes histone lactylation. To elucidate the effect of *STMN1* on histone lactylation, histones were extracted from DMS114 and H196 cells following *STMN1* knockdown or overexpression. The levels of Pan Kla and H3K18la were decreased upon *STMN1* knockdown and increased upon *STMN1* overexpression, demonstrating that *STMN1* promotes histone lactylation (Fig. 9A-D).

To explore the underlying mechanism, cellular lactate concentrations were measured and it was revealed that *STMN1* knockdown significantly reduced lactate levels, whereas *STMN1* overexpression increased lactate production (Fig. 9E-H), indicating that *STMN1* may regulate histone lactylation by modulating cell lactate generation.

To determine whether *STMN1* itself undergoes lactylation, co-IP and western blotting was performed. The results confirmed that *STMN1* was lactylated in both DMS114 and H196 cells, and its lactylation level was positively associated with its expression: *STMN1* knockdown decreased its lactylation, whereas *STMN1* overexpression increased it (Fig. 9I-L). Collectively, these findings indicated that *STMN1* may not only promote cellular lactate production and histone lactylation, but also undergoes lactylation itself.

Discussion

The present study investigated the association between lactate metabolism and lung cancer pathogenesis. The oncogenic role and regulatory mechanisms of *STMN1* in lung cancer were investigated by integrating MR analysis with multi-dimensional functional validation.

Traditional observational studies are limited by their inability to fully eliminate confounding factors and reverse causality. By contrast, the MR approach capitalizes on the random inheritance of genetic variants, offering robust evidence for causal inference between exposures and outcomes (34). Recently, the mechanisms underlying lactate and lactylation in cancer, along with their potential as therapeutic targets and clinical applications in cancer, have been increasingly elucidated (35-37). In this context, the current

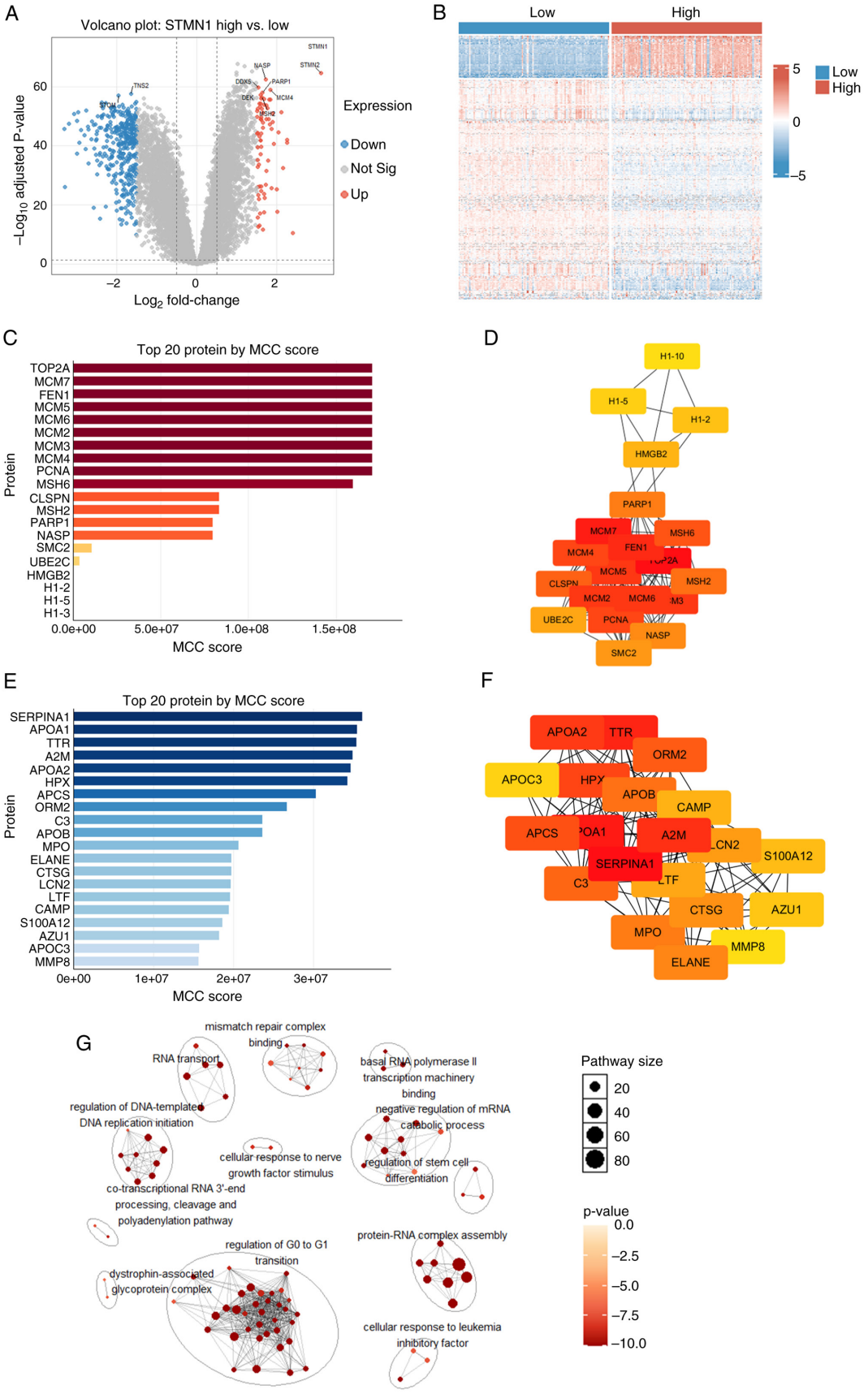

Figure 5. Identification and functional analysis of differentially expressed proteins in association with *STMN1*. (A) Volcano plot displaying proteins with differential expression between high and low *STMN1* expression groups. (B) Heatmap illustrating the expression profiles of 452 expression-divergent proteins. (C) Top 20 upregulated hub proteins, ranked by MCC scores as calculated in Cytoscape. (D) PPI network of the top upregulated hub proteins identified by MCC scoring, with nodes colored to represent functional modules. (E) Bar plot of the top 20 downregulated hub proteins, ranked by MCC scores calculated in Cytoscape. (F) PPI network of the top downregulated hub proteins identified by MCC scoring, with nodes colored to represent functional modules. (G) Dot plot of GO enrichment analysis for *STMN1*-associated proteins. Bubble size indicates the gene counts, and the color gradient denotes-$\log_{10}$(P-value). FC, fold change; GO, Gene Ontology; MCC, maximal clique centrality; PPI, protein-protein interaction; *STMN1*, Stathmin 1.

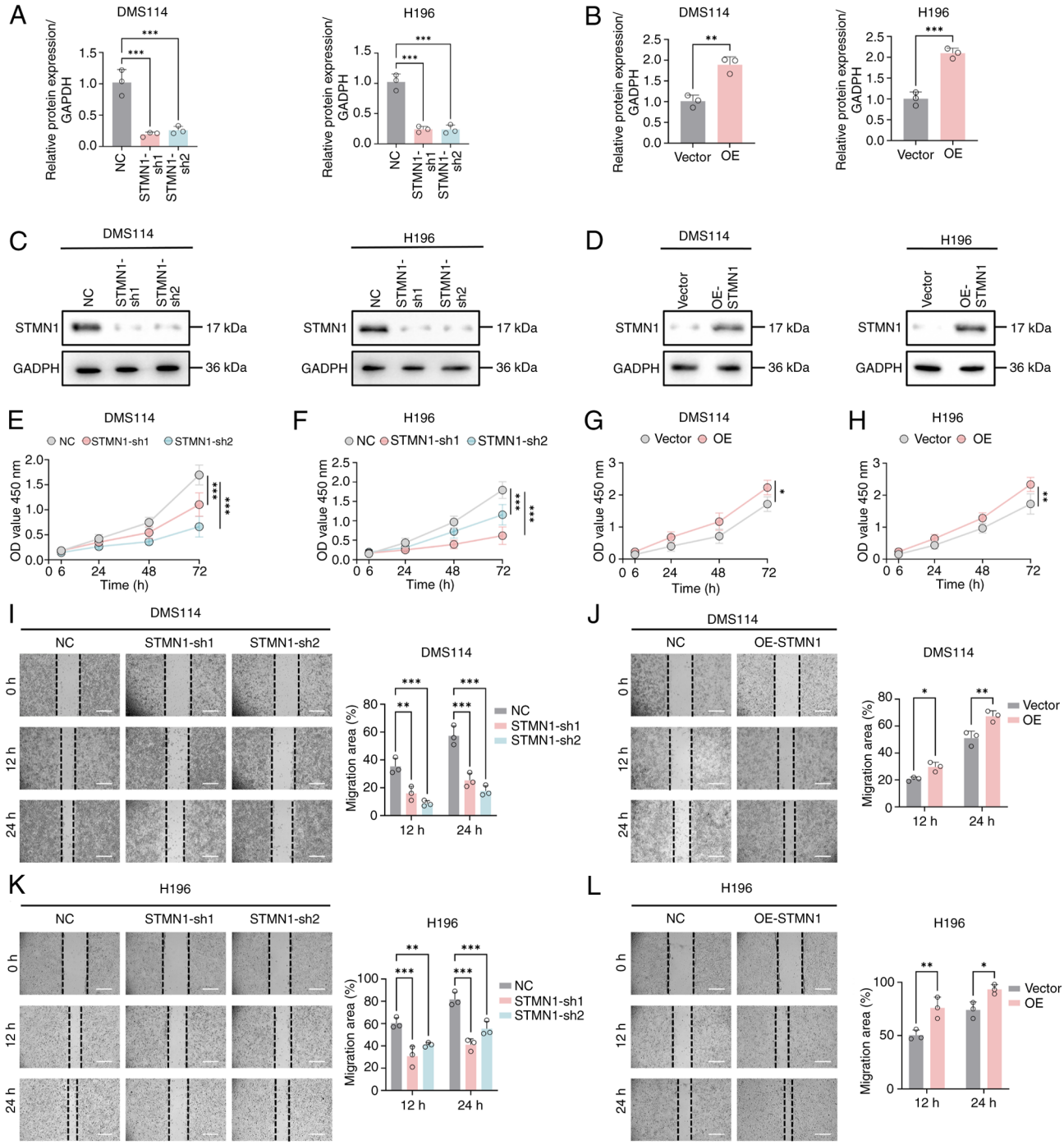

Figure 6. Effects of STMN1 on the proliferation and migration of DMS114 and H196 cells. (A) Western blot analysis was performed to assess STMN1 knockdown efficiency in DMS114 and H196 cells. (B) Western blot analysis was performed to assess STMN1 overexpression efficiency in DMS114 and H196 cells, with quantification of relative protein expression normalized to GAPDH. (C) Representative western blot images showing STMN1 protein expression in DMS114 and H196 cells following *STMN1* knockdown, with GAPDH used as a loading control. (D) Representative Western blot images showing STMN1 protein expression in DMS114 and H196 cells following *STMN1* overexpression, with GAPDH used as a loading control. (E) Proliferation of DMS114 and (F) H196 cells following *STMN1* knockdown. (G) Proliferation of DMS114 and (H) H196 cells following *STMN1* overexpression. (I) Migration of DMS114 cells following *STMN1* knockdown and (J) overexpression. (K) Representative wound healing assays showing the migration of H196 cells following *STMN1* knockdown. (L) Representative images and bar graph of wound healing assays showing the migration of H196 cells following *STMN1* overexpression. Scale bar, 300 μm. *P<0.05, **P<0.01, ***P<0.001. NC, negative control; OE, overexpression; sh, short hairpin; STMN1, Stathmin 1.

study sought to identify lactylation-related genes with a direct causal link to lung cancer. In the parallel analysis of multiple genes, multiple testing can increase the risk of false positives. Therefore, both FDR and Bonferroni multiple testing correction methods were implemented. Three core candidates were screened from 46 lactylation-related genes. Ultimately, only *STMN1* was confirmed to exhibit a significant association with lung cancer susceptibility, with an OR of 1.741. This finding suggested that elevated *STMN1* may serve as a key pathogenic driver of lung cancer.

As a microtubule-binding protein, STMN1 is involved in microtubule polymerization and depolymerization, and

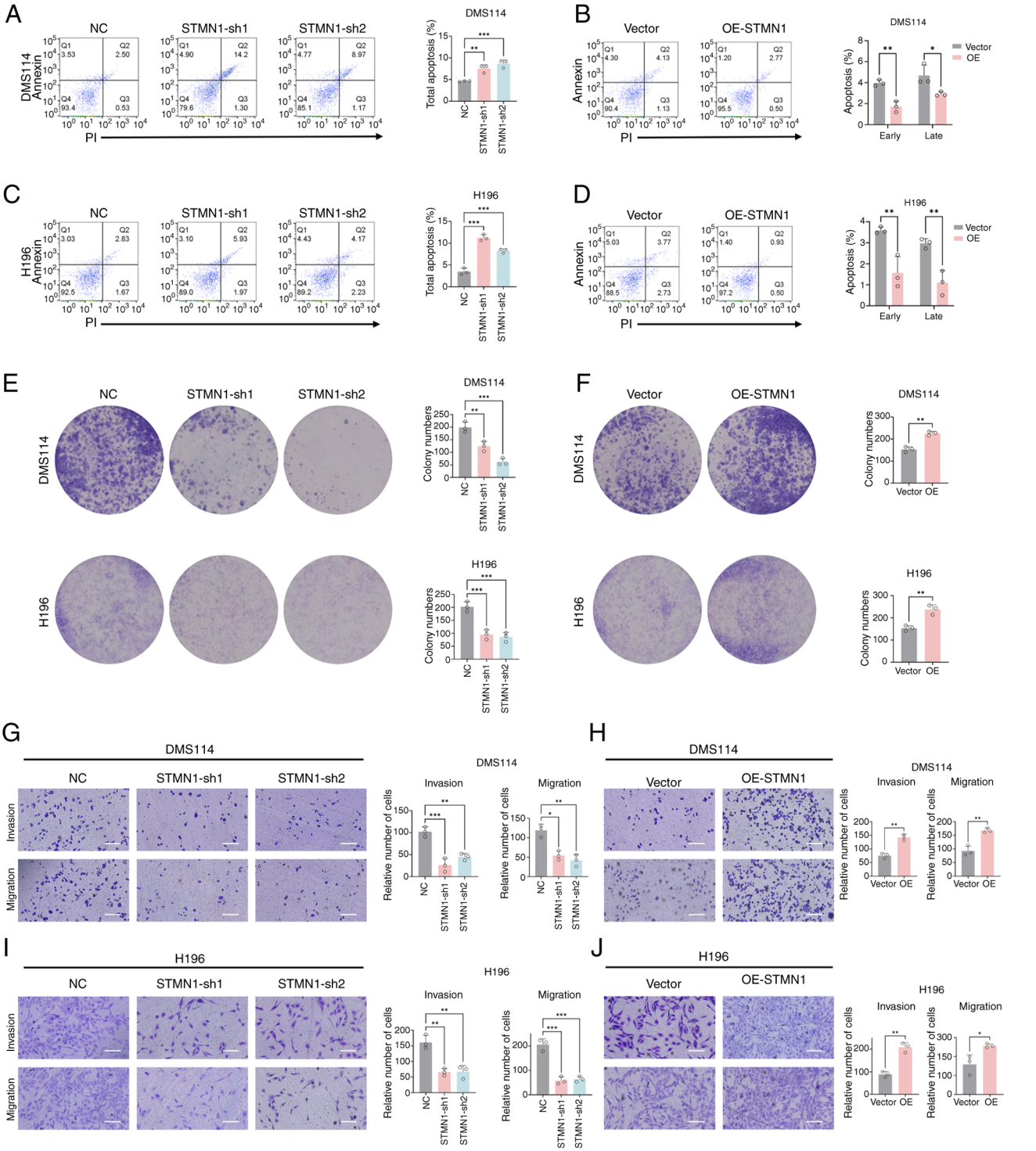

Figure 7. Effects of *STMN1* on apoptosis, colony formation, invasion and migration of DMS114 (human lung cancer cell line) and H196 (human lung sarcomatoid carcinoma cell line) cells. (A) Representative flow cytometry of Annexin V/PI staining for total apoptosis in DMS114 cells after *STMN1* knockdown. (B) Representative flow cytometric dot plots and bar graphs of Annexin V/PI staining for early and late apoptosis in DMS114 cells after STMN1 overexpression (OE-*STMN1*) compared with empty vector control (Vector). (C) Representative flow cytometric dot plots and bar graphs of Annexin V/PI staining for total apoptosis in H196 cells after *STMN1* knockdown (*STMN1*-sh1, *STMN1*-sh2) compared with negative control (NC). (D) Representative flow cytometric dot plots and bar graphs of Annexin V/PI staining for early and late apoptosis in H196 cells after *STMN1* overexpression (OE-*STMN1*) compared with empty vector control (Vector). (E and F) Representative images and bar graphs of colony formation assays: Colony formation of DMS114 cells after *STMN1* knockdown and OE. (G-J) Representative images and bar graphs of Transwell assays: Invasion and migration of DMS114 and H196 cells after *STMN1* knockdown and OE. Scale bar, 120 μm. *P<0.05, **P<0.01, ***P<0.001. NC, negative control; OE, overexpression; sh, short hairpin; STMN1, Stathmin 1.

participates in critical cellular processes, such as mitosis and apoptosis. Its upregulation in numerous tumor cells contributes to malignant phenotypes, including proliferation, migration and invasion (38,39). Numerous studies have indicated that increased *STMN1* expression is associated with unfavorable clinical outcomes in patients with prostate cancer (40),

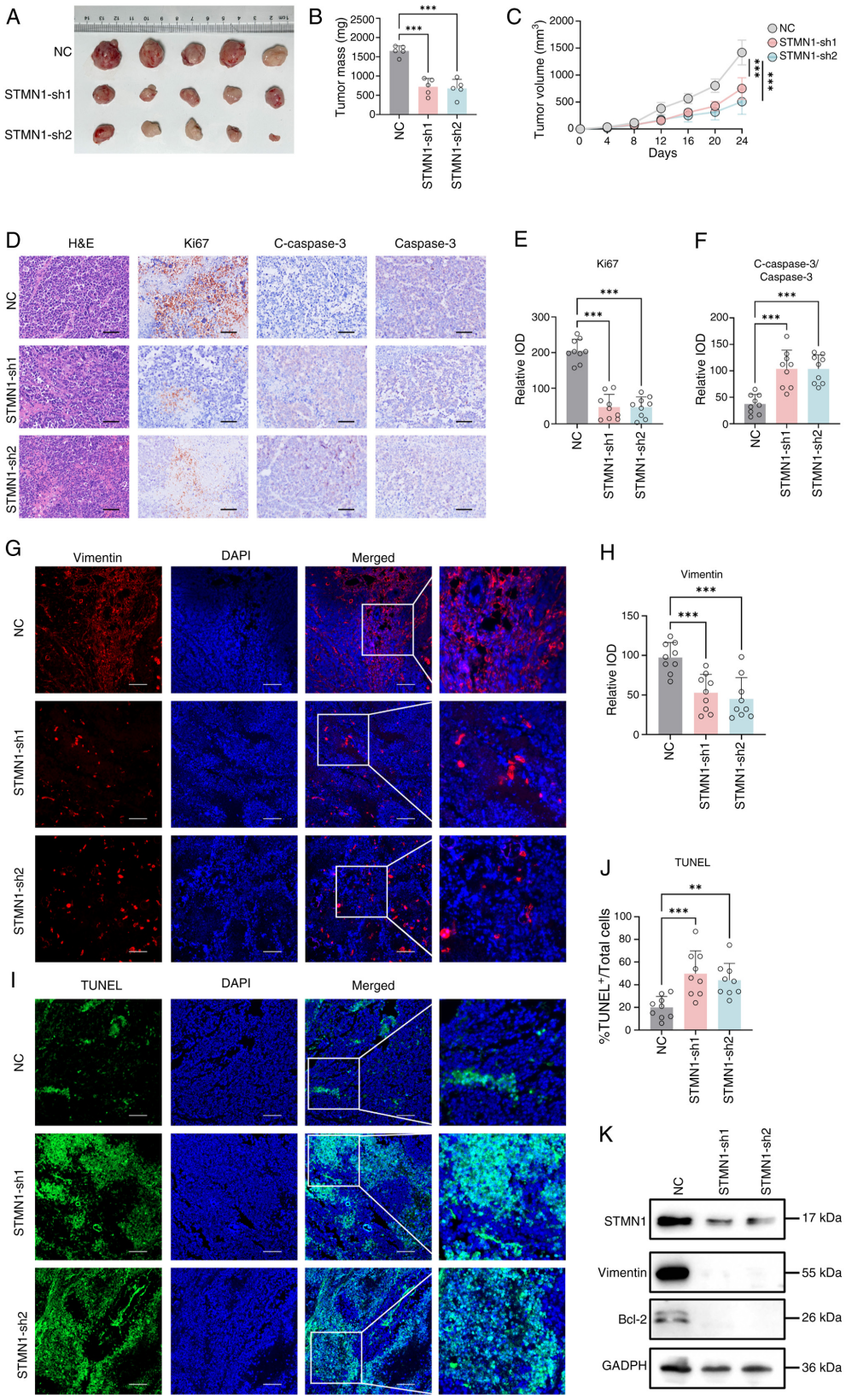

Figure 8. *STMN1* knockdown inhibits tumor growth *in vivo*. Tumor growth characteristics of the *STMN1*-sh1/sh2 and NC group: (A) Representative images of subcutaneous tumors are shown (n=5/group). (B) Bar graph of tumor weights. (C) Line graph of tumor volume growth. (D) Representative H&E staining and immunohistochemical staining for Ki67, C-Caspase-3, and Caspase-3 in NC, *STMN1*-sh1, and *STMN1*-sh2 groups. Scale bar, 50 μm. (E) Bar graph showing the relative IOD of Ki67 staining in NC, *STMN1*-sh1, and *STMN1*-sh2 groups. (F) Bar graph showing the relative IOD of C-Caspase-3 normalized to total Caspase-3 in NC, *STMN1*-sh1, and *STMN1*-sh2 groups. (G) Representative immunofluorescence staining of vimentin in tumor tissues from the NC, *STMN1*-sh1 and *STMN1*-sh2 groups. Scale bar, 50 μm. (H) Bar graph of the relative integrated optical density of Vimentin immunofluorescence staining. (I) Representative images of TUNEL staining in tumor tissues from the NC, *STMN1*-sh1 and *STMN1*-sh2 groups. Scale bar, 50 μm. (J) Proportion of TUNEL-positive cells relative to total cells in tumor tissues. (K) Western blot analysis verifying the expression of STMN1, Vimentin and Bcl-2 (anti-apoptotic protein) in tumor tissues. GAPDH served as a loading control. **P<0.01, ***P<0.001. C-Caspase-3, cleaved-Caspase-3; H&E, hematoxylin and eosin; MFI, mean fluorescence intensity; NC, negative control; sh, short hairpin; STMN1, Stathmin 1; IOD, Integrated Optical Density.

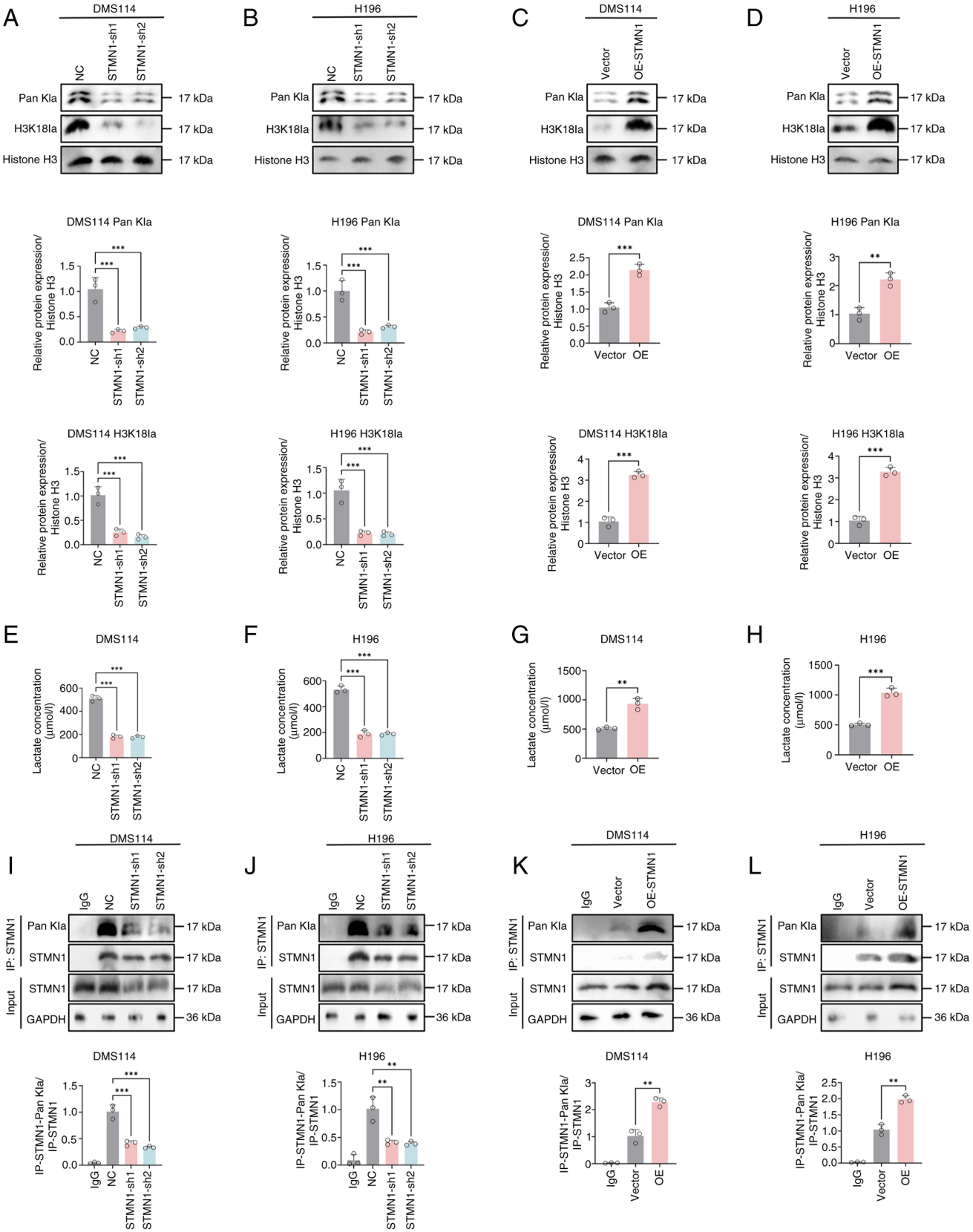

Figure 9. *STMN1* promotes histone lactylation and undergoes lactylation modification itself. (A) Western blotting of Pan Kla and H3K18la in DMS114 cells with *STMN1* knockdown (sh1, sh2) or NC, using Histone H3 as loading control. (B) Western blotting of Pan Kla and H3K18la in H196 cells with *STMN1* knockdown (sh1, sh2) or NC, using Histone H3 as loading control. (C) Western blotting of Pan Kla and H3K18la in DMS114 cells with *STMN1* OE) or vector control, using Histone H3 as loading control. (D) Western blotting of Pan Kla and H3K18la in H196 cells with *STMN1* overexpression (OE) or vector control, using Histone H3 as loading control. (E-H) Cellular lactate concentrations in DMS114 and H196 cells with *STMN1* knockdown or *STMN1*-OE was measured using a lactate assay kit, verifying the regulatory effect of *STMN1* on cellular lactate production. (I-L) Co-IP combined with western blotting was performed to validate the lactylation of STMN1 itself in DMS114 and H196 cells, and the effect of *STMN1* knockdown/overexpression on its own lactylation level was quantitatively analyzed, with IgG as the negative control and GAPDH as the input internal reference. **P<0.01, ***P<0.001. H3K18la, histone H3 lysine 18 lactylation; IP, immunoprecipitation; NC, negative control; OE, overexpression; Pan Kla, global histone lactylation; sh, short hairpin; STMN1, Stathmin 1.

gallbladder carcinoma (41), colorectal carcinoma (42), pancreatic cancer (43) and breast carcinoma (44). By contrast, *STMN1* can exert tumor-suppressive effects on bladder cancer (45), highlighting its context-dependent role in carcinogenesis. To date, to the best of our knowledge, the role of *STMN1* in lung cancer has not been explored. A previous study on hepatocellular carcinoma identified 16 lactylation-related prognosis-associated differentially expressed genes, including *STMN1,* by analyzing the gene expression profiles from The Cancer Genome Atlas database (46). Additionally, *STMN1* has been recognized as a marker of glycolysis (47), further linking its role to metabolic reprogramming in cancer. Elevated expression of immune checkpoint molecules can weaken antitumor immune reactions, thereby allowing the tumor to evade immune surveillance and promote disease advancement (48). The current study demonstrated that *STMN1* was significantly linked to an unfavorable prognosis in patients with lung cancer. Furthermore, high *STMN1* expression was correlated with reduced immune cell infiltration and lower immune scores in lung cancer tissues. These observations support the dual potential of *STMN1* as both a prognostic marker and a therapeutic target in lung cancer. The combination of *STMN1* inhibitors with ICIs may enhance the anti-lung cancer efficacy of ICIs, which could be related to the potential improvement of the TME immune status associated with *STMN1* downregulation. This hypothesis warrants further validation in future studies.

Using functional enrichment analysis, and *in vitro* and *in vivo* experiments, the present study initially elucidated the multi-dimensional mechanisms by which *STMN1* could promote lung cancer progression. GO enrichment analysis showed that proteins related to *STMN1* participated in G_0-G_1 cell cycle transition and negative regulation of mRNA catabolism. This suggested that *STMN1* may support the rapid proliferation of tumor cells through two parallel pathways: Accelerating cell cycle progression and ii) maintaining the stability of carcinogenesis-related mRNA. The former can shorten the time for lung cancer cells to switch from the quiescent phase to the proliferative phase, whereas the latter can sustain the continuous activation of oncogenic signaling pathways by inhibiting the degradation of tumor suppressor gene mRNAs (49).

Both cell-based and animal studies further validated the regulatory function of *STMN1* in cell functions and the TME. *STMN1* knockdown notably suppressed the proliferation, migration and invasion capabilities of DMS114 human lung cancer cells and H196 human lung sarcomatoid carcinoma cells, induced cell apoptosis, and downregulated the expression levels of the anti-apoptotic protein Bcl-2 and the EMT marker Vimentin. This result partially overlaps with the reported mechanism of *STMN1* in other tumors. For example, *STMN1* can promote cell migration by regulating microtubule dynamic stability in breast cancer (50). Consistent with these findings, the present study demonstrated that *STMN1* promoted EMT by upregulating vimentin expression in DMS114 and H196 cells. These results indicated that the pro-tumor and pro-metastatic function of *STMN1* is conserved across different cancer types, supporting the existence of universal oncogenic pathways regulated by *STMN1*.

In the present study, the enrichment ratio of oncogenic pathways, such as TP53 and Hippo signaling pathways, was notably greater in the high *STMN1* expression group compared with that in the low *STMN1* expression group. Additionally, DGIdb analysis revealed differences in the categories of druggable targets between the two groups, providing further insights into understanding the interaction between *STMN1* and other oncogenic pathways. For example, *STMN1* may enhance the resistance of lung cancer cells to apoptotic signals by activating TP53 mutation-related pathways. Meanwhile, the high enrichment of the Hippo signaling pathway could further amplify *STMN1*-mediated cell proliferation, forming an '*STMN1*-TP53-Hippo' synergistic oncogenic network. Thus, it may be hypothesized that the combined targeted intervention against this network (such as by using an *STMN1* inhibitor and a TP53 repair agent) might be more effective in inhibiting lung cancer progression compared with a single-target intervention, offering a molecular foundation for developing precise therapeutic regimens.

To further assess the functional link between *STMN1* and lactate metabolism, a series of mechanistic experiments were performed. First, intracellular lactate levels were measured in lung cancer cells with *STMN1* knockdown or overexpression, and it was revealed that *STMN1* positively regulated lactate production: Depletion of *STMN1* reduced lactate concentration, whereas its overexpression increased it. This result directly connects *STMN1* to the upstream metabolic process of lactate generation, which is the precursor for protein lactylation. Subsequently, it was confirmed that *STMN1* could promote Pan Kla and H3K18la in lung cancer cells, as evidenced by reduced lactylation levels after *STMN1* knockdown and enhanced lactylation after overexpression. Notably, the current study further verified that *STMN1* itself undergoes lactylation modification. These findings not only validate the role of *STMN1* as a lactylation-related gene, but also reveal a novel post-translational modification of *STMN1*, which may be involved in the feedback regulation of its oncogenic function. The newly discovered link between *STMN1* and lactate metabolism/lactylation further expands the mechanistic understanding. *STMN1* may promote lung cancer progression not only by regulating microtubule dynamics and cell cycle, but also by enhancing lactate production and subsequent protein lactylation, including its own self-lactylation. This dual regulatory mechanism suggests that *STMN1* acts as a key node connecting metabolic reprogramming and oncogenic signaling in lung cancer, which may explain its strong pathogenic effect in the current MR analysis.

Despite the rigorous design and reliable results of the present study, there are certain limitations. First, the exposure data for MR analysis were derived from eQTL databases, which may have constraints regarding sample scale and ethnic background. In the current study, the lung cancer GWAS datasets were derived from the Finnish population, whereas the eQTL effect of *STMN1* might vary across different ethnic groups. As no publicly available Asian or multi-ethnic lung cancer GWAS datasets with sufficient sample size and comprehensive genotype-phenotype annotations currently exist, the generalizability of the MR findings to non-European populations remains to be verified. In the future, we aim to validate the MR results in Asian or multi-ethnic cohorts once relevant datasets are released. Second, the study did not investigate the direct association between *STMN1*, lactate metabolism and histone lactylation in depth. As a lactylation-related gene, it remains unclear whether lactate metabolites regulate *STMN1* expression.

Subsequent verification using techniques such as metabolomics and chromatin immunoprecipitation-sequencing is required.

In conclusion, the present study clarified the causal association between *STMN1* and lung cancer using the MR method, and revealed its mechanism in regulating tumor cell functions and TME. The study provided a novel theoretical foundation for prognostic evaluation and targeted treatment of lung cancer. In the future, the clinical value of *STMN1* should be further verified to promote the development of related targeted drugs.

Acknowledgements

Not applicable.

Funding

This study was supported by the National Natural Science Foundation of China (grant no. 82472879).

Availability of data and materials

The data generated in the present study may be requested from the corresponding author.

Authors' contributions

YC, YZ and HW jointly conceptualized the study framework and designed the research protocols. HW and YZ performed *in vitro* and *in vivo* experiments, with HW assisting in data collection and preliminary sorting. SZ and SH led the bioinformatics analyses and interpreted the key results. YC drafted the initial manuscript, whereas SH and QZ conceived and designed the study, interpreted data, and revised the manuscript. FH and SZ supplemented experimental data and verified result reproducibility. All authors reviewed the manuscript and agreed to the submission, and all authors read and approved the final manuscript. YC and SH confirm the authenticity of all the raw data.

Ethics approval and consent to participate

The present study was approved by the Animal Experimentation Ethics Committee of the Huazhong University of Science and Technology (IACUC no. 4847; Wuhan, China).

Patient consent for publication

Not applicable.

Competing interests

The authors declare that they have no competing interests.

References

1. Singh A, Daemen A, Nickles D, Jeon SM, Foreman O, Sudini K, Gnad F, Lajoie S, Gour N, Mitzner W, *et al*: NRF2 Activation promotes aggressive lung cancer and associates with poor clinical outcomes. Clin Cancer Res 27: 877-888, 2021.
2. Zugazagoitia J, Osma H, Baena J, Ucero AC and Paz-Ares L: Facts and hopes on cancer immunotherapy for small cell lung cancer. Clin Cancer Res 30: 2872-2883, 2024.
3. Chen H, Deng C, Gao J, Wang J, Fu F, Wang Y, Wang Q, Zhang M, Zhang S, Fan F, *et al*: Integrative spatial analysis reveals tumor heterogeneity and immune colony niche related to clinical outcomes in small cell lung cancer. Cancer Cell 43: 519-536.e5, 2025.
4. Paz-Ares L, Dvorkin M, Chen Y, Reinmuth N, Hotta K, Trukhin D, Statsenko G, Hochmair MJ, Özgüroğlu M, Ji JH, *et al*: Durvalumab plus platinum-etoposide versus platinum-etoposide in first-line treatment of extensive-stage small-cell lung cancer (CASPIAN): A randomised, controlled, open-label, phase 3 trial. Lancet 394: 1929-1939, 2019.
5. Cui Y, Qiu T, Wang J, Liu X, Luo L, Yin J, Zhi X, Wang W, Feng G, Wu C, *et al*: IFITM3 enhances immunosensitivity via MHC-I regulation and is associated with the efficacy of anti-PD-1/-L1 therapy in SCLC. Mol Cancer 24: 187, 2025.
6. Lu Y, Li H, Zhao P, Wang X, Shao W, Liu Y, Tian L, Zhong R, Liu H and Cheng Y: Crosstalk between cancer-associated fibroblasts and non-neuroendocrine tumor cells in small cell lung cancer involves in glycolysis and antigen-presenting features. Mol Med 30: 274, 2024.
7. Boullier C, Lamaze FC, Haince JF, Bux RA, Orain M, Zheng J, Zhang L, Wishart DS, Bossé Y, Manem VSK and Joubert P: Metabolomic profiling of pulmonary neuroendocrine neoplasms. Cancers (Basel) 16: 3179, 2024.
8. Ding XJ, Mei T, Xi XN, Wang JY, Wang WJ, Chen Y, Lu YX, Qin TT and Huang DZ: ACT001 suppresses the malignant progression of Small-cell lung cancer by inhibiting lactate production and promoting Anti-tumor immunity. Thoracic Cancer 16: e70028, 2025.
9. Ma J, Tang L, Tan Y, Xiao J, Wei K, Zhang X, Ma Y, Tong S, Chen J, Zhou N, *et al*: Lithium carbonate revitalizes tumor-reactive CD8+ T cells by shunting lactic acid into mitochondria. Nat Immunol 25: 552-561, 2024.
10. Zhang D, Tang Z, Huang H, Zhou G, Cui C, Weng Y, Liu W, Kim S, Lee S, Perez-Neut M, *et al*: Metabolic regulation of gene expression by histone lactylation. Nature 574: 575-580, 2019.
11. Shang X, Cheng B, Zhang C, Zhao C, Wang R, Zhang X, Jiang D, Zhang X, Ma X, Mao H, *et al*: The LDH-H3K18La-Nur77 axis potentiates immune escape in small cell lung cancer. Adv Sci (Weinh) 12: e13608, 2025.
12. De Leo A, Ugolini A, Yu X, Scirocchi F, Scocozza D, Peixoto B, Pace A, D'Angelo L, Liu JKC, Etame AB, *et al*: Glucose-driven histone lactylation promotes the immunosuppressive activity of monocyte-derived macrophages in glioblastoma. Immunity 57: 1105-1123.e8, 2024.
13. Huang ZW, Zhang XN, Zhang L, Liu LL, Zhang JW, Sun YX, Xu JQ, Liu Q and Long ZJ: STAT5 promotes PD-L1 expression by facilitating histone lactylation to drive immunosuppression in acute myeloid leukemia. Signal Transduct Target Ther 8: 391, 2023.
14. Zhang C, Zhou L, Zhang M, Du Y, Li C, Ren H and Zheng L: H3K18 lactylation potentiates immune escape of Non-small cell lung cancer. Cancer Res 84: 3589-3601, 2024.
15. Larsson SC and Burgess S: Appraising the causal role of smoking in multiple diseases: A systematic review and meta-analysis of Mendelian randomization studies. EBioMedicine 82: 104154, 2022.
16. Li Y, Sundquist K, Zhang N, Wang X, Sundquist J and Memon AA: Mitochondrial related genome-wide Mendelian randomization identifies putatively causal genes for multiple cancer types. EBioMedicine 88: 104432, 2023.
17. Zhou L, Gao H, Zhang J, Xu Q, Wang Q, Wang L, Tan Y, Luo Z, Zhou J, Shuai H, *et al*: Metabolic syndrome and cancer risk: A two-sample Mendelian randomization study of European ancestry. Int J Surg 111: 311-321, 2025.
18. Wu J, Yang Z, Ding J, Hao S, Chen H, Jin K, Zhang C and Zheng X: Proteome-wide Mendelian randomization identifies causal plasma proteins in prostate cancer development. Hum Genomics 19: 17, 2025.
19. Zhang N, Li Y, Sundquist J, Sundquist K and Ji J: Identifying actionable druggable targets for breast cancer: Mendelian randomization and population-based analyses. EBioMedicine 98: 104859, 2023.
20. Yao W, Hu X and Wang X: Crossing epigenetic frontiers: The intersection of novel histone modifications and diseases. Signal Transduct Target Ther 9: 232, 2024.
21. Bao C, Ma Q, Ying X, Wang F, Hou Y, Wang D, Zhu L, Huang J and He C: Histone lactylation in macrophage biology and disease: From plasticity regulation to therapeutic implications. EBioMedicine 111: 105502, 2025.

22. Jiao Y, Ji F, Hou L, Lv Y and Zhang J: Lactylation-related gene signature for prognostic prediction and immune infiltration analysis in breast cancer. Heliyon 10: e24777, 2024.
23. Wang Y, Li P, Xu Y, Feng L, Fang Y, Song G, Xu L, Zhu Z, Wang W, Mei Q and Xie M: Lactate metabolism and histone lactylation in the central nervous system disorders: Impacts and molecular mechanisms. J Neuroinflammation 21: 308, 2024.
24. George J, Lim JS, Jang SJ, Cun Y, Ozretić L, Kong G, Leenders F, Lu X, Fernández-Cuesta L, Bosco G, *et al*: Comprehensive genomic profiles of small cell lung cancer. Nature 524: 47-53, 2015.
25. Cai L, Liu H, Huang F, Fujimoto J, Girard L, Chen J, Li Y, Zhang YA, Deb D, Stastny V, *et al*: Cell-autonomous immune gene expression is repressed in pulmonary neuroendocrine cells and small cell lung cancer. Commun Biol 4: 314, 2021.
26. Liu Q, Zhang J, Guo C, Wang M, Wang C, Yan Y, Sun L, Wang D, Zhang L, Yu H, *et al*: Proteogenomic characterization of small cell lung cancer identifies biological insights and subtype-specific therapeutic strategies. Cell 187: 184-203.e8, 2024.
27. Newman AM, Liu CL, Green MR, Gentles AJ, Feng W, Xu Y, Hoang CD, Diehn M and Alizadeh AA: Robust enumeration of cell subsets from tissue expression profiles. Nat Methods 12: 453-457, 2015.
28. Becht E, Giraldo NA, Lacroix L, Buttard B, Elarouci N, Petitprez F, Selves J, Laurent-Puig P, Sautès-Fridman C, Fridman WH and de Reyniès A: Estimating the population abundance of tissue-infiltrating immune and stromal cell populations using gene expression. Genome Biol 17: 218, 2016.
29. Racle J, de Jonge K, Baumgaertner P, Speiser DE and Gfeller D: Simultaneous enumeration of cancer and immune cell types from bulk tumor gene expression data. ELife 6: e26476, 2017.
30. Finotello F, Mayer C, Plattner C, Laschober G, Rieder D, Hackl H, Krogsdam A, Loncova Z, Posch W, Wilflingseder D, *et al*: Correction to: Molecular and pharmacological modulators of the tumor immune contexture revealed by deconvolution of RNA-seq data. Genome Med 11: 50, 2019.
31. Aran D, Hu Z and Butte AJ: xCell: Digitally portraying the tissue cellular heterogeneity landscape. Genome Biol 18: 220, 2017.
32. Griffith M, Griffith OL, Coffman AC, Weible JV, McMichael JF, Spies NC, Koval J, Das I, Callaway MB, Eldred JM, *et al*: DGIdb: Mining the druggable genome. Nat Methods 10: 1209-1210, 2013.
33. Jin Y, Xiao T, Feng Y, Yang J, Guo C, Hu L and Ji H: A mesenchymal-like subpopulation in non-neuroendocrine SCLC contributes to metastasis. J Genet Genomics 48: 571-581, 2021.
34. Li J, Tang M, Gao X, Tian S and Liu W: Mendelian randomization analyses explore the relationship between cathepsins and lung cancer. Commun Biol 6: 1019, 2023.
35. Li F, Si W, Xia L, Yin D, Wei T, Tao M, Cui X, Yang J, Hong T and Wei R: Positive feedback regulation between glycolysis and histone lactylation drives oncogenesis in pancreatic ductal adenocarcinoma. Mol Cancer 23: 90, 2024.
36. Li W, Zhou C, Yu L, Hou Z, Liu H, Kong L, Xu Y, He J, Lan J, Ou Q, *et al*: Tumor-derived lactate promotes resistance to bevacizumab treatment by facilitating autophagy enhancer protein RUBCNL expression through histone H3 lysine 18 lactylation (H3K18la) in colorectal cancer. Autophagy 20: 114-130, 2024.
37. Zhu R, Ye X, Lu X, Xiao L, Yuan M, Zhao H, Guo D, Meng Y, Han H, Luo S, *et al*: ACSS2 acts as a lactyl-CoA synthetase and couples KAT2A to function as a lactyltransferase for histone lactylation and tumor immune evasion. Cell Metab 37: 361-376.e7, 2025.
38. Zhang R, Gao X, Zuo J, Hu B, Yang J, Zhao J and Chen J: STMN1 upregulation mediates hepatocellular carcinoma and hepatic stellate cell crosstalk to aggravate cancer by triggering the MET pathway. Cancer Sci 111: 406-417, 2020.
39. Qian L, Cairong Z, Yongdong L Quan L, Haihu Z, Xiaofeng Z, Xuan Y, Yongcheng C, Kai C, Guanming L and Jie L: Prognostic role of STMN1 expression and neoadjuvant therapy efficacy in breast cancer. BMC Cancer 25: 453, 2025.
40. Ge S, Cen J, Liu X, Hong Y, Tang Y, Yu Y, Li H, Xie T, Wang C, Cai M, *et al*: TGFβ-activated Asporin interacts with STMN1 to promote prostate cancer docetaxel chemoresistance and metastasis by upregulating the Wnt/β-catenin signaling pathway. Drug Resist Updat 81: 101227, 2025.
41. Wang J, Ni X, Shen S, Zhang D, Ni X, Suo T, Lu P, Fan K, Liu H and Liu H: Phosphorylation at Ser10 triggered p27 degradation and promoted gallbladder carcinoma cell migration and invasion by regulating stathmin1 under glucose deficiency. Cell Signal 80: 109923, 2021.
42. Bi C, Cui H, Fan H and Li L: LncRNA LINC01116 promotes the development of colorectal cancer by targeting miR-9-5p/STMN1. Onco Targets Ther 13: 10547-10558, 2020.
43. Wang S, Su T, Tong H, Zhou D, Ma F, Ding J, Hao Y, Shi W and Quan Z: Circβ-catenin promotes tumor growth and Warburg effect of gallbladder cancer by regulating STMN1 expression. Cell Death Discov 7: 233, 2021.
44. Zhang Y, Wei S, Zhang Q, Zhang Y and Sun C: Paris saponin VII inhibits triple-negative breast cancer by targeting the MEK/ERK/STMN1 signaling axis. Phytomedicine 130: 155746, 2024.
45. Tan S, Kang Y, Li H, He HQ, Zheng L, Wu SQ, Ai K, Zhang L, Xu R, Zhang XZ, *et al*: circST6GALNAC6 suppresses bladder cancer metastasis by sponging miR-200a-3p to modulate the STMN1/EMT axis. Cell Death Dis 12: 168, 2021.
46. Cheng Z, Huang H, Li M, Liang X, Tan Y and Chen Y: Lactylation-related gene signature effectively predicts prognosis and treatment responsiveness in hepatocellular carcinoma. Pharmaceuticals (Basel) 16: 644, 2023.
47. Dai L, Fan G, Xie T, Li L, Tang L, Chen H, Shi Y and Han X: Single-cell and spatial transcriptomics reveal a high glycolysis B cell and tumor-associated macrophages cluster correlated with poor prognosis and exhausted immune microenvironment in diffuse large B-cell lymphoma. Biomark Res 12: 58, 2024.
48. Kong X, Zhang J, Chen S, Wang X, Xi Q, Shen H and Zhang R: Immune checkpoint inhibitors: Breakthroughs in cancer treatment. Cancer Biol Med 21: 451-472, 2024.
49. Chen W, Zhao W, Wu X, Fang T, Chen Z, Chen Z, Su W, Zhao X, Hu Y, Xu Y, *et al*: circFOXK2 Stabilizes STMN1 mRNA via PABPC1 to promote the progression of NSCLC. Cancer Med 14: e70729, 2025.
50. Liao L, Zhang YL, Deng L, Chen C, Ma XY, Andriani L, Yang SY, Hu SY, Zhang FL, Shao ZM and Li DQ: Protein phosphatase 1 subunit PPP1R14B stabilizes STMN1 to promote progression and paclitaxel resistance in Triple-negative breast cancer. Cancer Res 83: 471-484, 2023.